Planetary core formation via multispecies pebble accretion

G. Andama [ORCID],[1]★ N. Ndugu,[2,3]★ S. K. Anguma[3] and E. Jurua[1]★

[1]*Department of Physics, Mbarara University of Science and Technology, Mbarara, Uganda*
[2]*Center for Space Research, North-West University, Potchefstroom 2531, South Africa*
[3]*Department of Physics, Muni University, Arua, Uganda*

ABSTRACT

In the general classical picture of pebble-based core growth, planetary cores grow by accretion of single pebble species. The growing planet may reach the so-called pebble isolation mass, at which it induces a pressure bump that blocks inward drifting pebbles exterior to its orbit, thereby stalling core growth by pebble accretion. In recent hydrodynamic simulations, pebble filtration by the pressure bump depends on several parameters including core mass, disc structure, turbulent viscosity and pebble size. We have investigated how accretion of multiple, instead of single, pebble species affects core growth rates, and how the dependence of pebble isolation mass on turbulent viscosity and pebble size sets the final core masses. We performed numerical simulations in a viscous one-dimensional disc, where maximal grain sizes were regulated by grain growth, fragmentation and drift limits. We confirm that core growth rates and final core masses are sensitive to three key parameters: the threshold velocity at which pebbles fragment on collision, the turbulent viscosity and the distribution of pebble species, which yield a diversity of planetary cores. With accretion of multiple pebble species, planetary cores can grow very fast, reaching over 30–40 M_E in mass. Potential cores of cold gas giants were able to form from embryos initially implanted as far as 50 au. Our results suggest that accretion of multispecies pebbles could explain: the estimated 25–45 M_E heavy element abundance inside Jupiter's core; the massive cores of extrasolar planets; the disc rings and gaps at wider orbits; and the early and rapid formation of planetary bodies.

Key words: hydrodynamics – planets and satellites: formation – planets and satellites: gaseous planets – planets and satellites: physical evolution – protoplanetary discs – stars: formation.

1 INTRODUCTION

The theory of planet formation in protoplanetary discs (hereafter, PPDs) has developed by leaps and bounds ever since the monumental work of Safronov (1969). In one school of thought, planets may form by the gravitational collapse of a dense and dynamically cold gas disc (Kuiper 1951; Cameron 1978; Boss 1997; Gammie 2001; Rice et al. 2003; Tanga et al. 2004; Rafikov 2005; Durisen et al. 2007) followed by tidal downsizing (Nayakshin 2010). Gravitational collapse requires sufficiently massive discs and mainly favours the formation of giant planets at the disc outskirts (Boss 1997; Boley 2009; Armitage 2010).

In another school of thought, planets may also form oligarchically by the core accretion paradigm (Wetherill 1980; Kokubo & Ida 1998; Thommes, Duncan & Levison 2003; Coleman & Nelson 2014). Here, micrometre-sized dust grains in the natal PPDs first have to grow by coagulation into millimetre–centimetre (mm–cm) sized particles. These mm–cm sized particles may concentrate in some regions of the disc where they may gravitationally collapse into metre–kilometre sized bodies called planetesimals (e.g. Youdin & Goodman 2005; Johansen et al. 2007; Raettig, Klahr & Lyra 2015; Carrera, Johansen & Davies 2015). Planetesimals

larger than 100 km then form potential planetary embryos. These planetary embryos can also form through a different mechanism, for example, when collisions between smaller planetesimals result in a merger of over 100 km-sized planetesimals (e.g. Kokubo & Ida 2012). In the core accretion paradigm, the planetary embryos can then accrete smaller planetesimals to grow into a full planet (Safronov 1969; Mizuno, Nakazawa & Hayashi 1978; Mizuno 1980; Kokubo & Ida 2012). However, core growth via planetesimal accretion is typically slow unless most of the solid mass in the disc is converted into planetesimals less than 10 km in size (Tanaka & Ida 1999; Thommes et al. 2003; Levison, Thommes & Duncan 2010; Johansen & Bitsch 2019). Nevertheless, fast planetesimal-based core accretion rates were reported for planetesimals with a size less than 1 km (e.g. Mordasini, Alibert & Benz 2009a; Mordasini et al. 2009b), even though there is no evidence in the Solar system for planetesimals of such smaller sizes (Bottke et al. 2005a,b; Morbidelli et al. 2009; Singer et al. 2019).

A planetary core may also grow into a full planet by accreting aerodynamically coupled bodies via gas drag, popularly known as pebble accretion (Johansen & Lacerda 2010; Ormel & Klahr 2010; Lambrechts & Johansen 2012; Lambrechts, Johansen & Morbidelli 2014). Though the current framework of planet formation by core accretion of planetesimals or pebbles is the most successful, it cannot satisfactorily attribute the observed substructures at wider orbital

★ E-mail: gandama@must.ac.ug (GA); n.ndugu@muni.ac.ug (NN); ejurua@must.ac.ug (EJ)

locations to planets (Lodato et al. 2019; Ndugu, Bitsch & Jurua 2019; Nayakshin, Dipierro & Szulágyi 2019).

The formation of planetary bodies by the core accretion paradigm is strongly shaped by the availability and size distribution of solid material in the PPDs (see the review by Johansen et al. 2014). In particular, pebble accretion is constrained by the formidable radial drift barrier, which leads to the rapid loss of cm-sized solids on short dynamical time-scales (Whipple 1972; Weidenschilling 1977; Takeuchi & Lin 2005; Alexander & Armitage 2007; Brauer et al. 2007; Brauer, Dullemond & Henning 2008). Furthermore, Johansen, Ida & Brasser (2019) demonstrated that mm–cm sized dust material with a Stokes number larger than 0.1 is expected to drain on shorter time-scales than the disc's lifetime. Consequently, such rapid loss of dust grains can impede the formation of planetesimals and the subsequent growth of planetary cores by pebble accretion.

However, studies of PPDs from various surveys (e.g. Testi et al. 2003; Wilner et al. 2005; Rodmann et al. 2006; Brauer et al. 2007; Pérez et al. 2012; Trotta et al. 2013; Carrasco-González et al. 2016; Ansdell et al. 2017) indicate that a substantial amount of dust grains in the mm–cm range survive even in the discs that are in their late stages of evolution, contrary to theoretical predictions. The findings from the above surveys may not be globally true. In fact, a recent study by Tychoniec et al. (2020) revealed that most discs contain a small amount of pebbles and only few discs retain a substantial amount of pebbles. The retention of small dust grains in PPDs has been linked to the destructive collision of larger dust aggregates (Blum & Wurm 2008) and subsequent coagulation–fragmentation equilibrium (Dominik & Dullemond 2008). Birnstiel, Dullemond & Brauer (2009) demonstrated that the fragmentation of grains could facilitate dust retention in the disc. Also, zonal flows formed by magnetorotational instability (MRI; e.g. Johansen, Youdin & Klahr 2009; Dzyurkevich et al. 2010; Johansen, Klahr & Henning 2011; Uribe et al. 2011) can cause overdensities and hence pressure bumps that act as dust traps and help to retain dust grains in the outer region of the disc (Pinilla et al. 2012). Dust trapped in the pressure bumps induced by massive planets may also undergo fragmentation to produce finer grains (Drążkowska et al. 2019). The retention, evolution and distribution of grain sizes play an important role in planet formation models as they determine the outcome of the planetary bodies (Barrière-Fouchet et al. 2005), as well as the disc structure (Dullemond & Dominik 2004).

The grain size distribution can be approximated using either simple power-law fits as in the MRN model (Mathis, Rumpl & Nordsieck 1977) or the complex analytical approach of Birnstiel, Ormel & Dullemond (2011). Birnstiel, Klahr & Ercolano (2012) further developed a two-dust population model of dust size distribution, classifying the distribution into opacity bearing grains and larger grains. The subpopulation of the smaller grains determines the temperature profile and hence the disc structure (Dullemond & Dominik 2004; Savvidou, Bitsch & Lambrechts 2020).

The discussed observational surveys of dust disc and dust distribution simulations present some evidence for the existence of numerous dust species in PPDs, each with a unique spatio-temporal distribution of the Stokes number. The assortment of different grain sizes may point to the fact that core accretion proceeds by accretion of multiple pebble species.

However, previous works that studied core growth via pebble accretion (e.g. Guillot, Ida & Ormel 2014; Lambrechts & Johansen 2014; Lambrechts et al. 2014; Bitsch, Lambrechts & Johansen 2015; Morbidelli et al. 2015; Bitsch & Johansen 2017; Ndugu, Jurua & Bitsch 2018; Brügger et al. 2018; Johansen et al. 2019; Ndugu et al. 2019, 2021) were based on two standard prescriptions. First,

the studies used a single spatio-temporal dominant particle size or Stokes number, which is assumed to carry most of the solid mass. Dust coagulation models (e.g. Dullemond & Dominik 2005) predict rapid conversion of most of the dust into larger grains within very short time-scales compared with the disc lifetimes. The grain population can thus be modelled as consisting of small- and large-size grain populations, where most of the mass is carried by the large-size population (Birnstiel et al. 2012). Through coagulation–fragmentation equilibrium, grain sizes may attain quasi-stationary size distribution (Dullemond & Dominik 2005). A quasi-stationary size means that one is justified to use a single-size approach, especially when the resulting grain sizes in the distribution are very similar. Nevertheless, in this work, instead of a single pebble size or Stokes number, we have studied how grain size distributions reconstructed from the dust evolution model of Birnstiel et al. (2012) influence planetary core growth through accretion of different pebble species. This is because considering only dominant pebble species may not provide a complete picture of the final core masses and growth rates. This could be important, especially when several other pebble species in the distribution carry some considerable mass. Consequently, we can easily underestimate final core masses or growth times if some of the species that may also contain significant mass are neglected during core assembly, as may be the case in the single-species approach.

Secondly, core growth stops whenever a pressure bump is induced by the growing core, and hence the final core masses are fixed by the classical pebble isolation mass (Lambrechts et al. 2014, hereafter L2014). However, hydrodynamical simulations show that through turbulence, some pebble species can still diffuse through the pressure bump exerted by sufficiently massive cores and can even pass into gaps carved out by Jupiter-mass planets (Weber et al. 2018). As a result of turbulent diffusion, Bitsch et al. (2018, hereafter B2018) and Ataiee et al. (2018) further demonstrated that the pebble isolation mass might not be completely universal for all pebble species because smaller pebble species may overcome weaker pressure bumps. Therefore, this suggests that those pebble species that diffuse through the pressure bump may sustain core accretion for an extended period.

The grain size distribution as in the two-population model of Birnstiel et al. (2012) now provides an opportunity to study core accretion in the context of multiple dust species (Guilera et al. 2020; Venturini et al. 2020; Drążkowska, Stammler & Birnstiel 2021; Savvidou & Bitsch 2021; Schneider & Bitsch 2021). For instance, both Guilera et al. (2020) and Venturini et al. (2020) used a mass-weighted representative pebble size derived from the dust population of several species in their pebble accretion model, where the final core masses are fixed by the classical L2014 prescription. Using a full grain size distribution, Guilera et al. (2020) studied how giant planet cores can form by hybrid pebble and planetesimal accretion at pressure maxima. Venturini et al. (2020) focused on the formation of super-Earths inside the snow line. However, Schneider & Bitsch (2021) studied the heavy element content of giant planets, also based on full dust evolution, and they focused on the evolution of different chemical species rather than the physical size distributions as considered in this work.

Drążkowska et al. (2021), using a full size distribution, studied the impact of grain growth and fragmentation on the core growth rate while the planet accreted throughout at a particular radial location. This allowed them to exclusively study the actual impact of fragmentation on core growth. Hence, they performed a limited set of simulations and did not take into account many aspects of planet formation such as gas accretion and orbital migration, which are crucial for the final architecture of planetary systems. For instance,

inward migration could enable a core to reach pebble isolation mass much faster in the disc regions closer to the star where the isolation mass is lower. This then gives the planet a chance to accrete gas and grow into a gas giant. Lastly, in their work the core masses were measured based on the L2014 model without taking into account the diffusion of pebbles across the pressure bump, which may affect the final core mass as discussed in B2018.

In this study, we performed similar numerical simulations, but quite different from the one presented in Drążkowska et al. (2021). The major difference in our work is that we self-consistently reconstruct a distribution of pebble sizes, their corresponding masses and Stokes numbers after full dust evolution at every time-step during core growth. This allowed us to investigate the contribution of each individual grain species as opposed to the mass-averaged pebble flux model used in previous studies. Here, we focused on two major problems: how concurrent accretion of several pebble species may affect core growth; and how the dependence of the pebble isolation mass on turbulent viscosity and pebble sizes may determine the final core masses. All this is based on the two-population model of Birnstiel et al. (2012) and the size reconstruction recipe in Birnstiel et al. (2015). We did not perform hydrodynamic simulations of the pebble isolation mass because it is beyond the scope of this work but rather we used the formula from B2018 to calculate the final masses.

The rest of the paper is structured as follows. In Section 2, we describe the underlying disc model, the size distribution of particles and the core growth model. In Section 3, we explain the main numerical experiments that we performed. We present and discuss our results in Section 4. We then summarize our findings in Section 5.

2 THEORETICAL BACKGROUND

2.1 The disc evolution model

In order to provide a complete picture of our core accretion of the multiple pebble species model, we employed the two-population model of Birnstiel et al. (2012). Here, we only describe the key ingredients of the gas and dust evolution model that we adopted in our numerical simulations and we refer the reader to Birnstiel et al. (2009, 2011, 2012) and Birnstiel, Dullemond & Brauer (2010), for more detailed descriptions of dust size evolution.

In the simulations, the initial gas surface density Σ_g is calculated using the self-similar solution of Lynden-Bell & Pringle (1974) given by

$$\Sigma_g(r) \propto \left(\frac{r}{r_c}\right)^{-\gamma} \exp\left[-\left(\frac{r}{r_c}\right)^{2-\gamma}\right]. \tag{1}$$

Here, γ is the viscosity power-law index and r_c is the characteristic radius at an initial time t_0.

For dust evolution in the disc, we adopt the two-dust-population model of Birnstiel et al. (2012), where the dust surface density evolves according to the advection–diffusion equation:

$$\frac{\partial \Sigma_p}{\partial t} + \frac{1}{r}\frac{\partial}{\partial r}\left\{r\left[\Sigma_p \bar{u} - D_g \Sigma_g \frac{\partial}{\partial r}\left(\frac{\Sigma_p}{\Sigma_g}\right)\right]\right\} = 0. \tag{2}$$

Here, Σ_p is the dust and gas surface densities and D_g is the gas diffusivity. $\bar{u}$ is the velocity of the dust weighted by the mass of the two dust populations and is given by

$$\bar{u} = (1 - f_m)u_0 + f_m u_1, \tag{3}$$

where u_0 and u_1 are the radial velocities of the two small- and large-size grain populations, respectively, with representative sizes

a_0 and a_1, which are set by growth, drift and fragmentation limits as described in Birnstiel et al. (2012). Here, the mass fraction f_m of the large-size grain population at radial distance r is calibrated as 0.97 and 0.75 for drift- and fragmentation-limited regimes, respectively.

The radial velocities u_0 and u_1 are calculated as the sum of radial drift velocity and the radial velocity due to gas drag (Weidenschilling 1977):

$$u_i = -\frac{2\tau_i}{1 + \tau_i^2}u_\eta + \frac{1}{1 + \tau_i^2}u_g. \tag{4}$$

Here, u_g is the gas velocity, u_i ($i = 0, 1$) represents either u_0 or u_1, and τ_i is the corresponding Stokes number, which is discussed in Section 2.2. u_η is the headwind velocity (Weidenschilling 1977; Nakagawa, Sekiya & Hayashi 1986) given by

$$u_\eta = -\frac{1}{2}\frac{1}{\rho_g \Omega_K}\frac{\partial P}{\partial r}, \tag{5}$$

where ρ_g is the mid-plane gas density, P is the gas pressure and Ω_K is the Keplerian frequency. The gas velocity u_g is given by

$$u_g = c_s\sqrt{1.5\alpha_t}, \tag{6}$$

where c_s is the sound speed and α_t is the turbulence parameter.

2.2 Particle size distribution

The distribution of solids in PPDs depends on their aerodynamic properties characterized by friction time, t_f, given by (Whipple 1972; Weidenschilling 1977)

$$t_f = \frac{mv}{||F_D||}, \tag{7}$$

where m is the mass of the particle, v is the terminal velocity and $||F_D||$ is the gas drag force.

For small particles, it is usually convenient to express their degree of coupling with the gas in terms of the dimensionless Stokes number τ_s given by

$$\tau_s = t_f \Omega_K = \frac{\rho_\bullet R}{\rho_g h_g} = \frac{\rho_\bullet \pi R}{2\Sigma_g}, \tag{8}$$

where $\rho_\bullet$ is the material density, R is the particle size, Σ_g is the gas surface density and h_g is the gas scaleheight.

Bodies with a Stokes number $\tau_s > 1$ become increasingly less coupled to the gas or even decouple completely, and therefore are not well suited for core growth by aerodynamic drag in the settling regime. However, bodies with a Stokes number smaller than 0.001 have a short friction time and hence a long settling time that enables them to stay coupled to the gas during their gravitational encounter with the growing cores. Therefore, these particles mostly follow the gas streamlines and may not be accreted efficiently (Guillot et al. 2014; Johansen et al. 2019; Rosenthal & Murray-Clay 2020). Furthermore, as shown by Johansen et al. (2019), pebbles with a Stokes number ∼0.1 drift faster and are lost to the central star on short dynamical scales.

Particles settle towards the mid-plane depending on their size and material density and may also radially drift on time-scales that equally depend on their aerodynamic properties (Whipple 1972; Adachi, Hayashi & Nakazawa 1976; Weidenschilling 1977; Dullemond & Dominik 2004). For higher radial drift velocities, larger particles tend to concentrate more in the inner disc regions than the smaller particles (Barrière-Fouchet et al. 2005; Birnstiel et al. 2010, 2011; Testi et al. 2014). This results in vertical and radial stratification of particles (see Fig. 1).
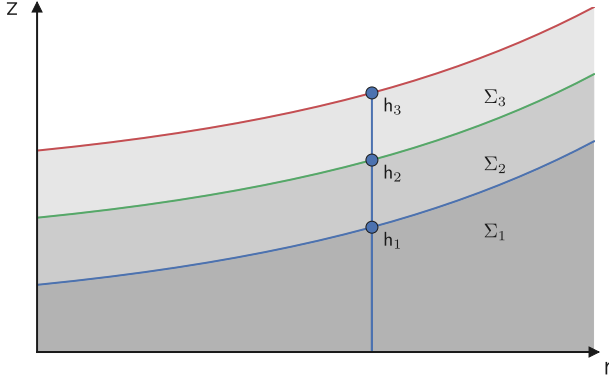
Figure 1. The geometry of vertical particle distribution used in our core growth model, where the particle species change from 1–3 with decreasing size.

In a quiescent disc, small dust grains are found to settle to the mid-plane, while the larger grains tend to oscillate about the mid-plane as their oscillation amplitude decays (Garaud, Barrière-Fouchet & Lin 2004). Here, we assume a simple model with N particle species, where particles sediment in a layered fashion with different scaleheights (Barrière-Fouchet et al. 2005). Particles with a small Stokes number stay in the upper layers of the gas disc, and those with a large Stokes number settle in the mid-plane, as depicted in the schematic diagram shown in Fig. 1. In this scenario, the scaleheight h_i (with $i = 1, 2, ..., N$ denoting different species) of each particle species is then calculated as (Youdin & Lithwick 2007)

$$h_i = \left(\frac{\alpha_t}{\tau_i}\right)^{1/2} h_g, \tag{9}$$

where τ_i is the Stokes number of a particular species.

The differential settling of particles discussed above suggests that the upper layers of the gas disc become relatively devoid of dust even for micrometre-sized grains (Dullemond & Dominik 2004). This motivates us to consider N different pebble species with surface densities, $\Sigma_{p,i}$. The simple MRN model of Mathis et al. (1977) describes grain size distribution quite well. However, we used the two-population model of Birnstiel et al. (2012) in our work, from which we reconstruct the grain sizes and their surface densities, $\Sigma_{p,i}$, as presented in Birnstiel et al. (2015). This is because we want to use a self-consistent size distribution, which takes into account the balance between the grain growth, fragmentation and drift barrier as described in Birnstiel et al. (2012).

Our grain sizes are distributed such that $R_{i+1} = 1.12R_i$, as in Birnstiel et al. (2011), where R_i is the size of the ith species. The dust surface density, $\Sigma_{p,i}$, corresponding to each species at a given radial distance and time is then reconstructed from gas surface density (Σ_g), dust surface density (Σ_p), fragmentation velocity (u_f), turbulent strength (α_t), material density ($\rho_\bullet$) and the disc mid-plane temperature (T) according to the recipe given in Birnstiel et al. (2015).

Laboratory experiments have constrained the fragmentation velocity threshold for silicate grains to be $u_f = 1 \ \mathrm{m\,s^{-1}}$ (Blum & Wurm 2008), while numerical simulations show that water-ice aggregates, which can grow to centimetre sizes, tend to fragment at much higher velocities of $u_f \geq 10 \ \mathrm{m\,s^{-1}}$ (Brauer et al. 2008; Wada et al. 2008; Gundlach et al. 2011; Gundlach & Blum 2015). Recent laboratory experiments by Musiolik & Wurm (2019) seem to suggest that ice and silicate grains have similar fragmentation velocities. However, the collisional outcomes also depend on the turbulent strength, the internal density of the solid bodies and the

local temperature, which can lead to a wide range of particle sizes. Lastly, the corresponding Stokes number, τ_i, of each pebble species from the reconstructed size distribution is then calculated using equation (8)

2.3 Dominant size distribution

In the two-population model of Birnstiel et al. (2012), the surface densities Σ_0 and Σ_1 of the small and large populations at a radial distance r are calculated as

$$\Sigma_0 = \Sigma_p(r)[1 - f_m(r)], \tag{10}$$

$$\Sigma_1 = \Sigma_p(r)f_m(r). \tag{11}$$

In typical classical pebble accretion scenarios, a single representative size is assumed to contain most of the dust mass, for example, in the large population. In this classical picture, we can calculate the mass-averaged dominant size R_d for the reconstructed size distribution as (Guilera et al. 2020; Venturini et al. 2020)

$$R_d = \frac{\sum_i \epsilon_i R_i}{\sum_i \epsilon_i}, \tag{12}$$

where

$$\epsilon_i = \frac{\Sigma_{p,i}}{\Sigma_g} \left(\frac{\alpha_t + \tau_i}{\alpha_t}\right)^{1/2}. \tag{13}$$

The corresponding Stokes number for the dominant species with size R_d can then be obtained by using equation (8).

2.4 Core growth model

In our planetary growth model, planetary embryos start accreting pebbles at the transition mass where Hill accretion becomes more efficient than the Bondi regime (Lambrechts & Johansen 2012). For the governing equations, we start from the classical pebble accretion rate of a dominant pebble species i in the two-dimensional (2D) Hill regime given by (Morbidelli et al. 2015)

$$\dot{M}_{2D} = \begin{cases} 2\,(\tau_i/0.1)^{2/3}\,\Omega_K r_H^2 \Sigma_{p,i} & (\tau_i < 0.1) \\ 2\Omega_K r_H^2 \Sigma_{p,i} & (\tau_i \geq 0.1) \end{cases}, \tag{14}$$

where r_H is the Hill radius.

The 2D solid accretion takes place when the effective accretion radius is greater than the particle scaleheight; otherwise, the core grows by three-dimensional (3D) accretion. Because the protoplanets are initially small, their gravitational reach is mostly below the particle scaleheight and hence the accretion rate follows the 3D mode. The 3D and 2D accretion modes are then related as in Morbidelli et al. (2015) by

$$\dot{M}_{3D} = \left[\sqrt{\frac{\pi}{8}} \left(\frac{\tau_i}{0.1}\right)^{1/3} \frac{r_H}{h_i}\right] \dot{M}_{2D}. \tag{15}$$

Here, we can calculate the critical core masses at which accretion switches from 3D to 2D as

$$M_{3D2D} = 4.06 \times 10^5 \times \alpha_t^{3/2} \tau_i^{-5/2} \left(\frac{H}{r}\right)^3 M_E, \tag{16}$$

where H/r is the disc's aspect ratio. Hence, the core accretion rate of the ith pebble species is given by

$$\dot{M}_{core,i} = \begin{cases} \dot{M}_{2D} & \text{for } \sqrt{\frac{\pi}{8}} \left(\frac{\tau_i}{0.1}\right)^{1/3} r_H > h_i \\ \dot{M}_{3D} & \text{otherwise} \end{cases}. \tag{17}$$
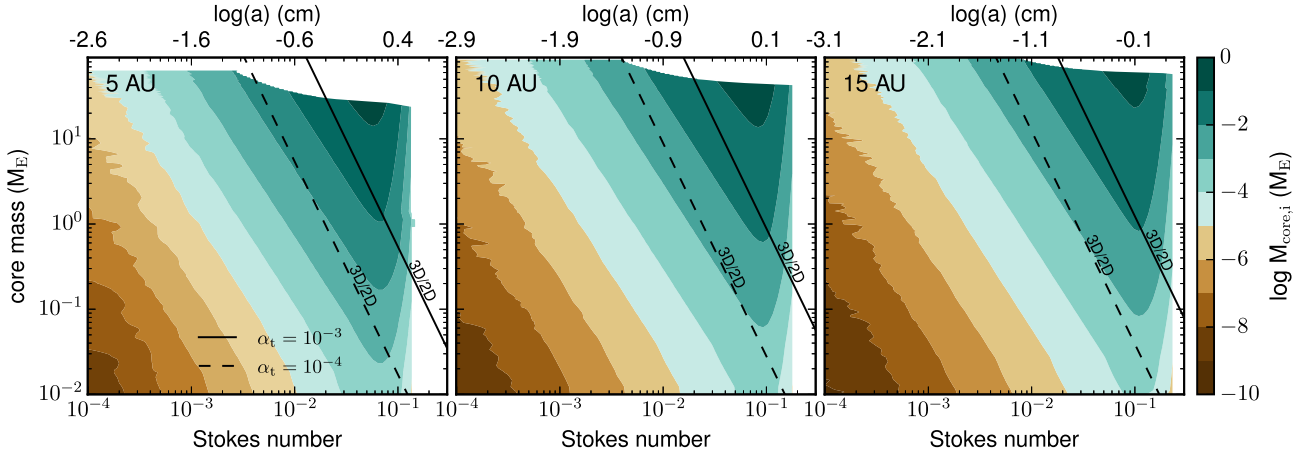
Figure 2. The planet mass at which pebble accretion switches from 3D to 2D as a function of the Stokes number, for $\alpha_t = 10^{-3}$ and $\alpha_t = 10^{-4}$. The colour scale shows the mass $M_{\text{core},i}$ accumulated by the planet from the ith pebble species, which is what each pebble species contributed to the final planet mass.

In Fig. 2, we illustrate the mass at which a growing planet switches from 3D to 2D accretion as a function of pebble size at 5, 10 and 15 au for turbulent strengths of $\alpha_t = 10^{-3}$ and $\alpha_t = 10^{-4}$. In the first place, the switch from 3D to 2D in discs with low turbulence occurs at a lower core mass, and the converse is true for discs with high turbulence. This is because in a less turbulent disc the pebble scaleheights are low, which increases the r_H/h_i ratio at a fixed r_H and hence constant core mass. Secondly, the accretion of smaller pebbles transitions from a 3D to 2D mode at higher core masses. For the case of larger pebbles, this transition occurs at much lower core masses. This is because, for the same turbulence strength, larger pebbles typically settle closer to the mid-plane and hence have low scaleheights compared with the smaller pebbles.

Also in Fig. 2, the contribution of particles of a given Stokes number to the total mass is shown by the colour plot, computed using equation (17). Here, pebble distributions were taken from the grain size reconstruction method described in more detail in Section 3. From the illustration in Fig. 2, pebbles with smaller Stokes number do not significantly contribute to the total core mass. For example, at 5 au, pebbles with a Stokes number less than 0.001 contribute roughly less than 10^{-4} M_E to a planetary core of 40 M_E. This is because the smaller pebbles are not easily accreted compared with the large pebbles, which carry most of the mass.

2.5 Pebble isolation mass

As the core grows massive enough, at some point it will begin to open a gap and induce a pressure bump at the outer edge of the gap where pebbles become trapped (Paardekooper & Mellema 2006; Morbidelli & Nesvorny 2012). Consequently, at a critical mass usually referred to as the pebble isolation mass, the core stops accreting pebbles (L2014; B2018; Ataiee et al. 2018).

However, recent hydrodynamical simulations suggest that pebbles with a small Stokes number can still cross to the inner disc through a gap carved out by a Jupiter-mass planet (see Weber et al. 2018, and references therein), where pebbles with a larger Stokes number are more efficiently filtered out. As the pressure bump scales with planet mass, where typical pebble isolation masses are an order of magnitude lower than a Jupiter-mass planet (Morbidelli & Nesvorny 2012; Lambrechts et al. 2014; Bitsch et al. 2018), the growing cores may not efficiently filter smaller pebbles. The

smaller pebbles may thus overcome the pressure and hence be accreted.

The pebble isolation mass, as originally developed by L2014 without consideration of turbulent effects, is given by

$$M_{\text{iso}} = 20 \left(\frac{H/r}{0.05} \right)^3 M_E \, . \tag{18}$$

B2018 and Ataiee et al. (2018) built on L2014 and investigated the pebble isolation mass taking into account turbulent diffusion and they obtained similar results where turbulence can significantly change pebble isolation mass. It is possible to use either formulation to study core growth by pebble accretion, where the resulting core masses should only differ by a factor of 1.5–2, as discussed in Ataiee et al. (2018). However, the B2018 and L2014 prescriptions give very similar results in the limit of weak turbulence, compared with Ataiee et al. (2018). Hence, for consistence, we follow B2018 because we have used classical model of L2014 to compare the final core masses with and without diffusion of pebbles across the pressure bump. B2018 derived an expression for pebble isolation mass with diffusion as

$$M_{\text{iso}} = M_{\text{iso}}^{\dagger} + \frac{\Pi_{\text{crit}}}{\lambda} M_E \, , \tag{19}$$

where $M_{\text{iso}}^{\dagger}$ is the pebble isolation mass without diffusion, Π_{crit} is the critical pressure gradient parameter, and λ defines the change in slope of pressure gradient inside the pressure bump generated by the planet. $M_{\text{iso}}^{\dagger}$, Π_{crit} and λ are given by

$$M_{\text{iso}}^{\dagger} = 25 f \, M_E, \qquad \lambda \approx \frac{0.00476}{f}, \qquad \Pi_{\text{crit}} = \frac{\alpha_t}{2\tau_i}. \tag{20}$$

Here, f is a fit to the isolation mass given by

$$f = \left[\frac{H/r}{0.05} \right]^3 \left\{ 0.34 \left[\frac{\log(\alpha_3)}{\log(\alpha_t)} \right]^4 + 0.66 \right\}$$

$$\times \left[1 - \frac{(\partial \ln P / \partial \ln r) + 2.5}{6} \right], \tag{21}$$

where $\alpha_3 = 0.001$ is the scaling factor and $\partial \ln P / \partial \ln r$ is the pressure gradient.

From equations (19), (20) and (21), we can calculate the pebble isolation mass with turbulent diffusion, $M_{\text{iso},i}$, for each pebble species
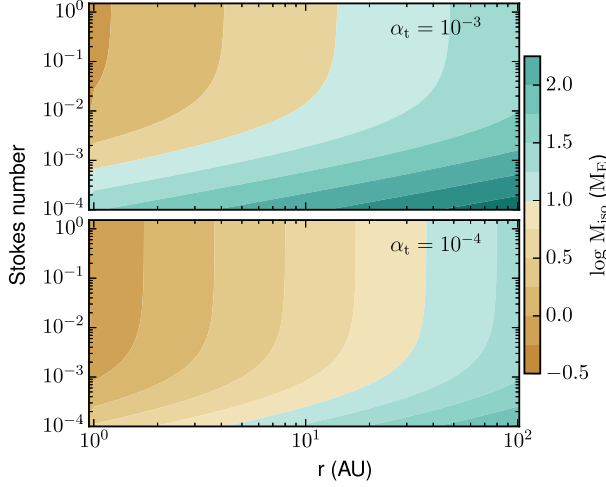
Figure 3. The pebble isolation mass as a function of pebble size and orbital distance for nominal disc turbulence parameters $\alpha_t = 10^{-3}$ and $\alpha_t = 10^{-4}$.

as

$$M_{iso,i} = 17.51 \left(\frac{H/r}{0.05} \right)^3 \left\{ 0.34 \left[\frac{\log(\alpha_3)}{\log(\alpha_t)} \right]^4 + 0.66 \right\}$$
$$\times \left(3.5 - \frac{\partial \ln P}{\partial \ln r} \right) \left(0.238 + \frac{\alpha_t}{\tau_i} \right) M_E. \tag{22}$$

To put equation (22) in perspective, the dependence of pebble isolation mass on grain size, turbulence viscosity and orbital distance is illustrated in Fig. 3. For each grain species, the isolation mass increases with orbital distance, and with turbulence levels. Additionally, at a particular radial distance, pebble isolation mass increases with decreasing Stokes number because, from equation (22), pebble isolation mass is inversely related to the Stokes number.

As a consequence of equation (22), a growing planet may block pebbles at different stages, as illustrated in Fig. 4; the figure shows which pebble species a non-migrating planet accretes as it reaches different masses. For example, at 5 au, a 20-M_E planet is accreting all pebble species. When the planet reaches 60 M_E, it has blocked all pebble species to the right of the dashed vertical line and can only accrete pebbles to the left of the vertical line. At higher orbital distances, the planet needs to grow bigger before it can start filtering larger pebbles.

2.6 Planetary migration scheme

We implement orbital evolution during core growth and follow the Paardekooper, Baruteau & Meru (2011) prescription, where cores experience Lindblad and corotation torques Γ_L and Γ_C, respectively, with the total torque Γ_{tot} given by

$$\Gamma_{tot} = \Gamma_L + \Gamma_C. \tag{23}$$

Here, the Lindblad torque is expressed as

$$\frac{\gamma \Gamma_L}{\Gamma_0} = -2.5 - 1.7\beta + 0.1s, \tag{24}$$

where $\gamma = 1.4$ is the adiabatic index, and s and β are the negatives of radial gradients of gas surface density, Σ_{pla}, and the temperature, T, respectively, calculated at the planet's location, r_{pla}. Γ_0 is expressed
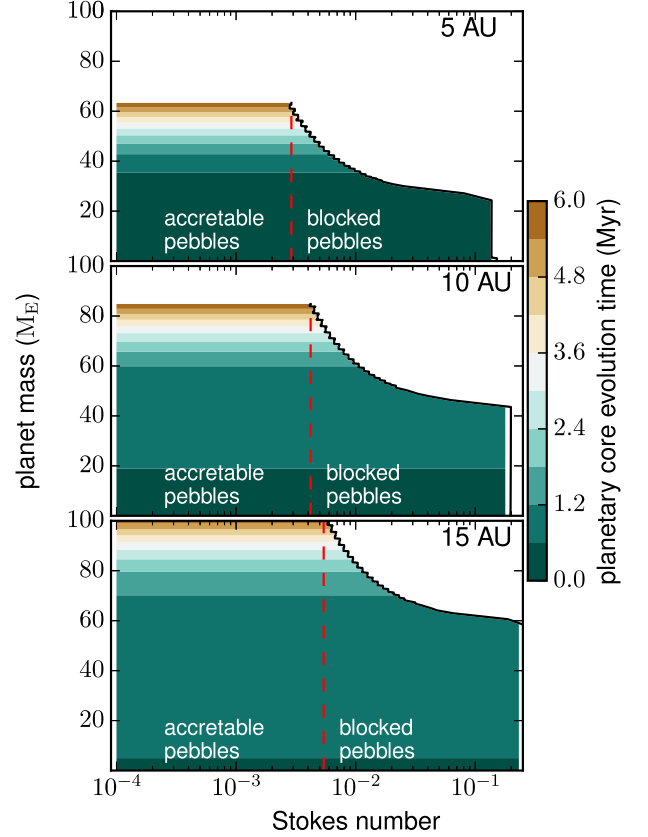

Figure 4. An illustration of how, using equation (22), a growing and non-migrating planet may filter pebbles with different Stokes numbers at 5, 10 and 15 au for a nominal disc turbulence parameter of $\alpha_t = 10^{-3}$, fragmentation velocity of 10 m s^{-1} and dust-to-gas ratio of 0.01, where grain sizes were obtained from the method described in Section 3.

as

$$\Gamma_0 = \left(\frac{q}{H/r} \right)^2 \Sigma_{pla} r_{pla}^4 \Omega_{pla}^2, \tag{25}$$

where q is the planet–star mass ratio, Ω_{pla} is the Keplerian frequency and the disc aspect ratio H/r is calculated at the planet's location. The corotation torque, which is induced by material corotating with the planetary body, is composed of barotropic and entropy-related parts. For a detailed discussion, we refer the reader to the review by Baruteau et al. (2014). The corotation torque is calculated using the formula (Paardekooper et al. 2010)

$$\frac{\gamma \Gamma_C}{\Gamma_0} = 1.1 \left(\frac{3}{2} - s \right) + 7.9 \frac{\xi}{\gamma}, \tag{26}$$

where the first and second terms are the barotropic and entropy components of the corotation torque and $\xi = \beta - (\gamma - 1)s$ is the radial entropy gradient.

In our model, we only incorporate type I migration but not type II because our model is limited to solid core growth just before pebble isolation mass, making type II migration unnecessary.

3 NUMERICAL SIMULATIONS

The full dust size population in Birnstiel et al. (2010, 2011, 2012) features a large number of different dust species, broadly classified into small and large dust size populations. Some of these species are

either accretable or just contribute to the disc opacity, which then determines the temperature profile of the disc.

We incorporated the two-population dust evolution code of Birnstiel et al. (2012)[1] in our numerical code for dust evolution. In the simulations, particles evolve in both time and space as the disc evolves, governed by balance between grain growth, fragmentation and drift size limits. We then reconstructed the surface density of each particle species for a sample of 150 species at every time-step, using the size distribution reconstruction code of Birnstiel et al. (2015).[2]

We performed our simulations in an axisymmetric 1D disc, with 200 logarithmically spaced radial grid points. For the global disc evolution, the computational grid extends from 0.05 to 3000 au with characteristic radius, $r_c = 200$ au, while we implant 0.01 M_E planetary embryos between 1 and 50 au. The central star has mass $M_* = 1.0$ $M_\odot$, temperature $T_* = 5778$ K, and radius $R_* = 1.0$ $R_\odot$. We assume a disc mass, $M_{disc} = 0.1$ $M_\odot$, which gives $\sim$330 M_E of dust mass for a nominal solid-to-gas ratio of 0.01. This is within the range of dust masses measured in different star-forming regions, especially for some Class 0 disc systems (see Manara et al. 2019; Tychoniec et al. 2020).

In the simulations, we tested three different initial dust-to-gas ratios, $f_{DG} = 0.01$, 0.015 and 0.02 with the following combinations of fragmentation velocity and turbulence parameter:

$$u_f = 10\,\mathrm{m\,s^{-1}}, \quad \alpha_t = 10^{-3};$$
$$u_f = 10\,\mathrm{m\,s^{-1}}, \quad \alpha_t = 10^{-4};$$
$$u_f = 1\,\mathrm{m\,s^{-1}}, \quad \alpha_t = 10^{-3};$$
$$u_f = 1\,\mathrm{m\,s^{-1}}, \quad \alpha_t = 10^{-4}.$$

Here, the turbulence parameter α_t regulates grain size in the fragmentation regime, pebble scaleheight and migration, which all change at the same time when α_t changes. The disc temperature is assumed to be constant in time and varies only with radial distance as defined in the two-population code.

We performed two sets of simulations. In the first set, we adopted the classical core accretion of the dominant pebble size where the isolation mass is governed by the classical equation (18) of L2014. In our dominant species model, we used the full size distribution to calculate the mass averaged Stokes number and the surface density corresponding to the dominant size, as described in Section 2.3.

In the second set, we fed the full size distribution into the core accretion routine, where pebbles of a given Stokes number are accreted independently. In this scenario, the pebble isolation mass of the individual species is set by equation (22) of B2018, and we calculate the accretion rates according to the recipe described in Appendix B. Furthermore, we terminate the accretion of the full size distribution and measure the planet mass when the core has reached the isolation mass of pebble species with Stokes number $\approx$0.001. This is because, as we saw in Fig. 2, the contribution of pebbles with a Stokes number less than 0.001 is small and stopping their accretion after the isolation mass of pebbles with Stokes number $\approx$0.001 is reached will not significantly affect our results.

Migration of planetary cores also takes place during core growth. We terminate core growth when the planet has migrated to 0.05 au or when it has reached the pebble isolation mass. If the core fails to reach pebble isolation mass, growth continues until the end of the time evolution of the disc.

[1]https://github.com/birnstiel/two-pop-py
[2]https://github.com/birnstiel/Birnstiel2015_scripts

4 RESULTS AND DISCUSSION

We present and discuss results for the two pebble accretion models. We start by discussing the classical scenario of core growth with dominant size distribution, where the isolation mass is determined by equation (18). Here, the dominant sizes were obtained by computing the mass-averaged dust size and Stokes number from the full grain size distribution reconstructed from the two-population model (Birnstiel et al. 2012). Then, we present results of our model featuring concurrent accretion of multiple pebble species, where the pebble isolation mass is controlled by equation (22). We then point out the differences between the two models and discuss what it means for formation of planetary systems by the core accretion paradigm in relation to current observations. Although the transition mass is sensitive to the initial position of the embryo, throughout our work, we assumed embryos with a transition mass $0.01 M_E$ for all initial orbital positions considered here.

4.1 Core growth with dominant pebble species

Fig. 5 represents core growth time-scales and final masses that were obtained from core growth using the accretion of the dominant pebble size. Here, we show results for different sets of fragmentation velocity and turbulence parameter. The plots in the top and bottom rows represent the final core masses and total growth times, respectively, as a function of the starting positions of the embryos. Here, we determined at what initial orbital positions our planetary embryos can grow and reach pebble isolation mass. From the plots, the planetary cores that took 2 Myr had not reached their pebble isolation mass. We note here that migration of planetary cores also took place during the entire process of core growth (their final orbital distances and growth times are discussed in more detail in Section 4.3).

From Fig. 5, our simulations with $u_f = 1$ m s^{-1} and $\alpha_t = 10^{-3}$ produced no significant growth of planetary embryos over the 2 Myr of disc evolution. This is because low fragmentation velocities in turbulent discs keep overall grain sizes small and more coupled to the gas, which makes their accretion difficult. Accretion becomes even more difficult when planetary cores are very small, where small dust grains simply drift past the embryo (Guillot et al. 2014). This is because the small embryos do not have strong enough gravitational force to pull off small grains that are strongly attached to the gas.

For the simulations performed with fragmentation velocity of 10 m s^{-1}, and turbulence strengths of 10^{-3} and 10^{-3}, planetary cores reached pebble isolation mass only when growth of the embryos started at a radial distance within 20 au for a nominal dust-to-gas ratio of 0.01. The corresponding growth time-scales for the cores implanted within 20 au to reach their isolation mass range between 0.1–1.5 Myr, as shown in the bottom panels of Fig. 5.

With increasing dust-to-gas ratio, core growth is boosted and planetary embryos that are introduced as far as 35 au can now reach the pebble isolation mass. At each initial radial distance, the growth time-scales are also greatly improved when the dust-to-gas ratio increases. The improved growth rates at higher dust-to-gas ratios can be related to the higher dust surface densities that allow cores to grow faster and bigger. Furthermore, radial drift motions of dust also depend on the dust-to-gas ratio, which, when increased, can bring about fast inward transport of solid material from the outskirts of the disc. This then increases pebble flux and accretion efficiency at the planet's location, and hence the embryos may effectively grow bigger with reduced growth time.

From Fig. 5, where $\alpha_t = 10^{-4}$ and $u_f = 1$ m s^{-1}, we registered much better final core masses in comparison with the other models.
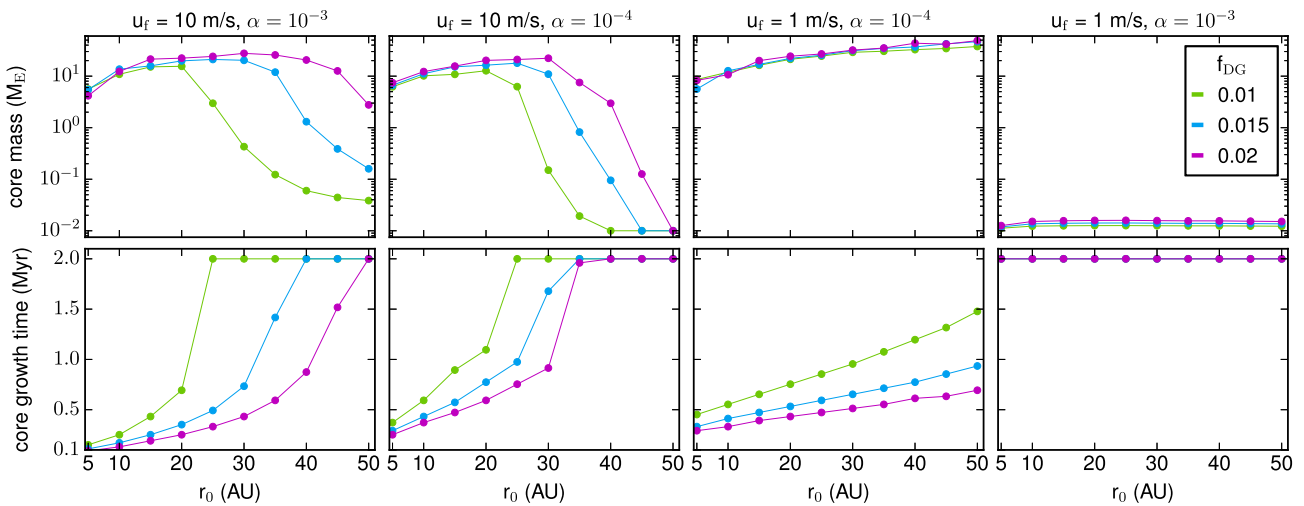
Figure 5. Top panels: the final core masses as a function of the starting position resulting from the accretion of the dominant pebble species. The dominant pebble size is calculated from the reconstructed pebble size distribution as derived from the full dust evolution model prescribed in Birnstiel et al. (2012). Core growth is measured within a period of 2 Myr of the gaseous disc life-span for different combinations of fragmentation velocity and turbulence levels. The final planetary cores become increasingly more massive if the dust-to-gas ratio f_{DG} increases from 0.01 to 0.02. Bottom panels: the corresponding total growth times of the planetary cores for the same values of parameters in the top panels. The planetary cores with growth times below 2 Myr reached their pebble isolation mass, and the growth time to reach isolation mass reduces with increasing dust-to-gas ratio.

Here, planetary cores can grow to 20–30 M_E when the cores start growing at orbital distances beyond 20 au. This is contrary to what has so far been reported in most pebble accretion models based on the dominant size approach, where it is difficult to grow such massive cores when planetary embryos start at wider orbits. Furthermore, many of these studies have predicted that pebble accretion is either too efficient or inefficient, depending on the prevailing physical conditions in the disc. However, in our simulations, we may attribute such massive core sizes to the fact that low fragmentation velocities keep grain sizes small. These small-size grains migrate to the inner disc regions slowly compared with larger grains and may last longer in many parts of the disc, thereby promoting core growth especially at large orbital distances.

In our simulations, the growth time-scales to reach pebble isolation mass typically span from ~0.2 to 1.8 Myr, as shown in the bottom panel of Fig. 5. This depends on the initial location of the embryo and the dust-to-gas ratio, where in the inner disc regions the cores take a shorter time to grow to their isolation mass. This is because the pebble isolation mass, as found by L2014 and B2018, is a cubic function of the disc aspect ratio, which increases with orbital distances. Thus, cores that grow at far orbital distances require more time and material to reach isolation mass (for a more detailed discussion, see Bitsch et al. 2015).

4.2 Core growth with full grain size distribution

In Fig. 6, we present the planetary core masses resulting from accretion of the full dust size distribution, where the sizes of different dust species were reconstructed using the grain size reconstruction recipe of Birnstiel et al. (2015). In the simulations, we used the pebble isolation mass with diffusion to separate pebble species for which the isolation mass has been attained. This ensures that when the planet has reached the isolation mass of a particular pebble species, that species is not accreted again during the rest of the core growth period. In Fig. 6, we overplot the results of the dominant species model presented in Fig. 5 for purposes of comparison with the multispecies model.

From Fig. 6, in the multiple pebble species approach, the core masses increase substantially in comparison with our dominant species approach. This is because the cores accrete not just a single pebble species but a variety of pebble species, where growth is sustained by accretion of smaller pebbles even after the larger pebbles have been isolated. We note here that the sustained growth is a consequence of each pebble species being isolated at different core masses due to the dependence of pebble isolation on the pebble Stokes number (see equation 22). Consequently, the core takes more time to grow than in the case of single species model. In the latter case, accretion stops as soon as the planet just reaches its classical pebble isolation mass, and hence the planets have shorter growth times. We discuss this in detail in Section 4.4.

Keeping the fragmentation velocity at 10 m s^{-1} and reducing the turbulence strength to $\alpha_t = 10^{-4}$, we obtain final core masses that are much smaller than those obtained from the model with turbulence level $\alpha_t = 10^{-3}$. Here, the growth patterns in both the single and multiple pebble species models are very similar. This is because the low turbulence level has three main effects. First, it allows a larger grain size distribution, which settles more efficiently toward the mid-plane. Secondly, the larger grains drift much faster than the smaller grains produced in a more turbulent disc. The former effect would result in better accretion efficiency, but then this could be counteracted by fast drifting grains, which could result in significant loss of the larger grain. Thus, all in all, for 10 m s^{-1} and $\alpha_t = 10^{-4}$, the cores may accumulate much smaller material and take a lot more time to reach the pebble isolation mass in such an environment. Thirdly, low turbulence levels reduce the turbulent diffusion of grains across the pressure bump. Hence, in this case, the pebble isolation mass with diffusion approaches the classical case without diffusion (Ataiee et al. 2018; Bitsch et al. 2018). Here, the pebble isolation mass is smaller than the case where turbulence strength is greater, hence resulting in smaller core masses. This is further illustrated in Fig. 7, where for $\alpha_t = 10^{-4}$, pebbles with a Stokes number greater 0.01 can be isolated by very similar planet masses (shown by red labels on the vertical lines). This also explains why the final core masses in both the dominant
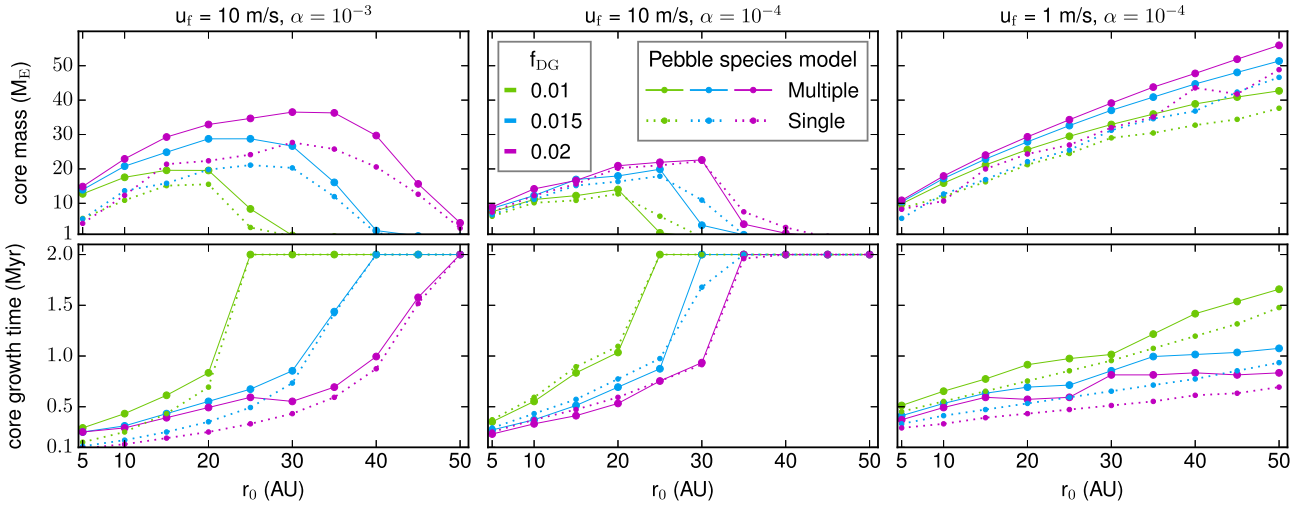
Figure 6. The final core masses (top panels) and the total growth time (bottom panels) as a function of the starting position, resulting from the concurrent accretion of multiple pebble species considering the full pebble size distribution. The plots have the same meaning as in Fig. 5. Here, the same single species model from Fig. 5 is overplotted for comparison with concurrent accretion of the full size distribution model. The planets in these plots migrate, and their growth tracks are shown in Fig. 9.
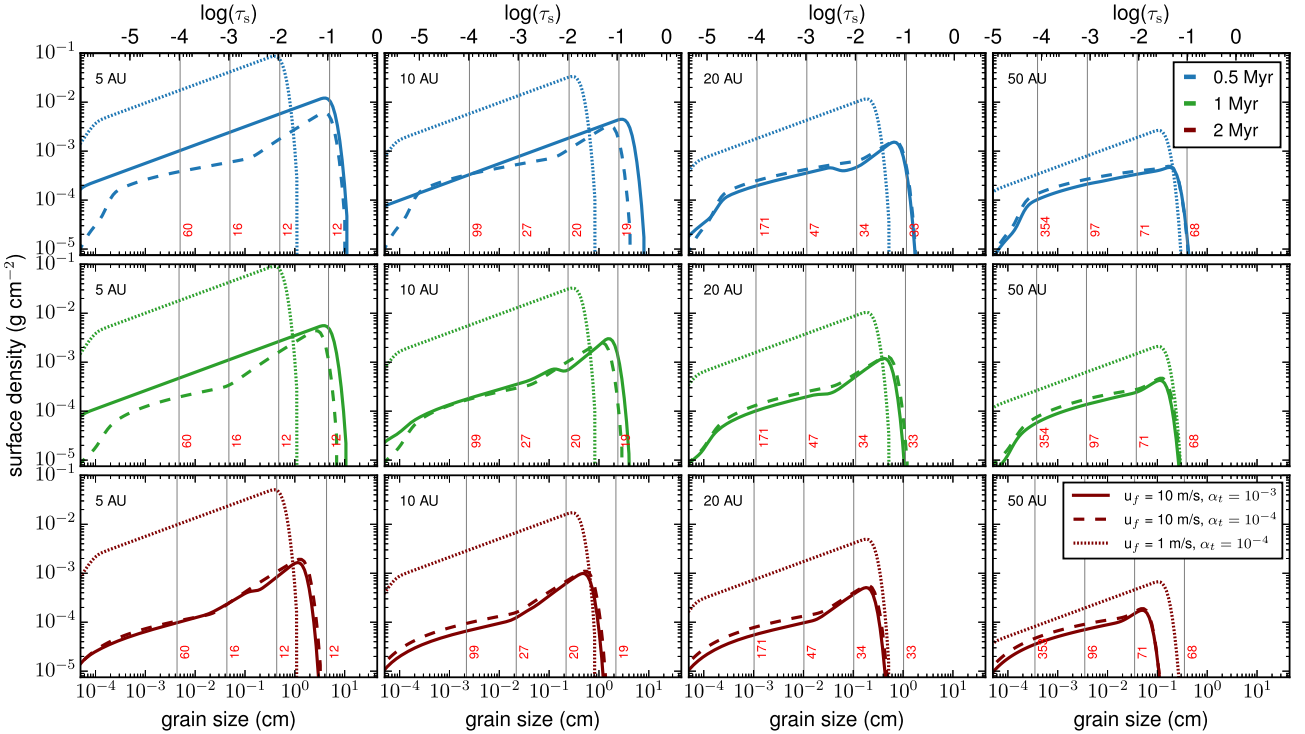
Figure 7. Grain size distribution reconstructed after 0.5 Myr (top row), 1 Myr (middle row) and 2 Myr (bottom row) of disc evolution for nominal $f_{DG} = 0.01$. We derived the grain size distributions using $\alpha_t = 10^{-3}$ with $u_f = 10$ m s^{-1} (solid line), $\alpha_t = 10^{-4}$ with $u_f = 10$ m s^{-1} (dashed line) and $\alpha_t = 10^{-4}$ with $u_f = 1$ m s^{-1} (dotted line). The Stokes numbers corresponding to the grain sizes are indicated on the upper axis. The grain sizes were reconstructed from the two-population model of Birnstiel et al. (2012) where dust evolution is governed by growth, fragmentation and drift limits. Here, the large population carries 0.75 and 0.97 of the solid mass in the fragmentation and drift limits, respectively (for details, see Appendix A). The vertical lines show pebble species that would be blocked at a planetary mass labelled on each line. The line labels are pebble isolation masses with diffusion corresponding to $\alpha_t = 10^{-4}$. Here, all pebble species on the right of the vertical line would be blocked.

and multispecies models in the middle panels of Fig. 6 are very similar.

With $u_f = 1$ m s^{-1} and $\alpha_t = 10^{-4}$, we obtained supermassive cores in the same way as the case of single species model, as shown on the right panels of Fig. 6. To further understand this trend, we refer

to the grain size distributions shown in Fig. 7. First, as demonstrated in Fig. 7, a fragmentation velocity of 1 m s^{-1} keeps pebbles at much smaller sizes, which thus drift at lower speeds than larger pebbles produced when the fragmentation limit is set to 10 m s^{-1}. Consequently, the small and slow-drifting pebbles live much longer

(possibly everywhere in the disc) than the larger pebbles, which may drain much more quickly. This creates opportunity for core growth at wider orbits. For example, from Fig. 7, the grain size distribution remains more stable after 1 Myr of disc evolution for our disc model with $\alpha_t = 10^{-4}$ and $u_f = 1$ m s^{-1} compared with the other two models. Secondly, the low turbulence ensures that the small pebbles are not stirred too far from the mid-plane.

From the above discussion, this implies that in the disc model with $\alpha_t = 10^{-4}$ and $u_f = 1$ m s^{-1}, pebbles are kept within the feeding zone of the core, possibly most of the time. The cores can then continue to accrete the small pebbles for an extended period of time. This suggests that at low disc turbulence and low fragmentation velocities, core growth from pebble accretion might be possible even in the last stages of the disc lifetime.

We note that the classical dominant species approach relies on the premise that the grain population containing the biggest solid mass budget constitutes grains of very similar aerodynamic size. This can be true if turbulence, fragmentation and grain growth conspire rightly to keep grains at very similar sizes. Consequently, in such an environment where grain size distribution can be similar, our multiple pebble species approach should yield very similar core masses as the classical dominant species model, possibly at faster growth rates.

In addition, our multispecies model requires two conditions: (i) the grains need to have varied size distribution with dissimilar aerodynamic properties and (ii) turbulence is required to operate in such a way as to enforce dependence of the pebble isolation mass on the pebble Stokes number. The first condition leads to a departure from the classical dominant species model because the different grain species are now subjected to different gas drag, which underpins pebble accretion. The second condition is required for sustaining core growth from smaller pebbles after the larger pebbles have been isolated. This holds only if the pebble isolation mass is not supposedly universal for all pebble species at a given radial location.

In our simulations, core growth rates and the final core masses are sensitive to the dust-to-gas ratio, fragmentation velocity and turbulence strength with the incorporation of the full grain size distributions. This gives a diverse outcome of final core masses, as shown in Fig. 6.

It should be noted that the masses in Fig. 7 do not directly correspond to the masses in Fig. 6. This is because in Fig. 6, we show the planet mass as a function of the starting position. However, the orbital distances in Fig. 7 are sample distances at which we constructed grain size distributions, and at which we showed sample isolation masses to illustrate at what mass pebble species may be blocked. Therefore, because we incorporated orbital migration, we need the final orbital distances (see Fig. 9) if we wish to relate the core masses in Fig. 6 to the isolation masses in Fig. 7. Furthermore, according to our multispecies accretion model, accretion stops once pebbles with $\tau_i = 0.001$ are blocked, as explained in Section 3. This means that the final core mass is determined by the pebbles with a Stokes number closest to 0.001. Because this Stokes number may be slightly greater than 0.001, the final core mass may not necessarily correspond to the isolation mass for the Stokes number 0.001 indicated in Fig. 7, but closer to it.

4.3 Growth tracks of planetary cores

Fig. 8 represents the time evolution of the planetary cores that grow via the multispecies accretion paradigm and initially implanted at orbital positions shown in Fig. 6. The corresponding orbital evolution is shown in Fig. 9 for a nominal dust-to-gas ratio of 0.01.

In Figs 8 and 9, the points where the growth tracks flatten show the points of growth saturation, and consequently there is no significant increase in mass. This occurs when the majority of pebble species have been isolated, but the core continues to slowly accrete the remaining pebble species with the smallest Stokes numbers. It is important to remember that, in our simulations, the final mass of the planet is determined when it reaches the isolation mass of pebbles with Stokes number ≈ 0.001. This then sets the final core growth time of the planets. In our results, the contribution of pebbles with small Stokes number close to 0.001 is negligibly small as reported in several studies (e.g. Guillot et al. 2014; Johansen et al. 2019). This is shown by the flattening of mass–time curves for the growing cores (see Fig. 8). The growth tracks that end at 2 Myr of disc evolution pertain to cores that have not yet reached their pebble isolation masses.

In Fig. 8, planetary cores accrete more efficiently in the moderately turbulent disc where we set $u_f = 10$ m s^{-1} and $\alpha_t = 10^{-3}$ compared with the models for which the turbulence parameter is set to $\alpha_t = 10^{-4}$. The apparent reasons for the differences in the growth times for these models are associated with the particle size distribution regulated by growth, fragmentation and turbulence, as previously discussed in Section 4.2.

With $u_f = 10$ m s^{-1} and $\alpha_t = 10^{-4}$, the grain size distribution mostly constitutes larger grains that drift faster compared with the other two models. This means smaller material availability and hence slower core growth rates, as most of the larger grains are lost on short time-scales via radial drift. This results in a relatively slow growth and hence longer growth times compared with the other two models, as shown in Fig. 8, especially for initial orbital positions between 10 and 20 au.

The size distribution produced by $u_f = 1$ m s^{-1} and $\alpha_t = 10^{-4}$ is typically in the millimetre range. These smaller sized dust grains are accreted less efficiently, resulting in extended growth times before the cores reach pebble isolation mass. However, concurrent accretion of these smaller multiple pebble species allows the planet to reach pebble isolation mass well before the 2 Myr of disc evolution, even for wider initial orbital locations.

Because the final core masses are determined by the pebble isolation mass for the smaller pebbles, we would expect longer growth times because of the slow accretion rates of these small pebbles. However, initially, the accretion of larger pebbles is more efficient than the smaller pebbles whose accretion rate increases as the core grows bigger. Also, the concurrent accretion of different species helps the core to rapidly increase in mass in a much shorter time. Thus, the smaller pebbles can now be accreted much more efficiently, thereby shortening the time for the planet to reach the isolation of the smallest species.

In Fig. 9, we show the core growth trajectories for the same sets of parameters as in Fig. 8. Here, planetary cores that were able to reach the pebble isolation mass migrated significantly inward. However, the fast growth rates of some cores propel them to reach pebble isolation mass after migrating over relatively short orbital distances. For example, for the models with low turbulence level of $\alpha_t = 10^{-4}$, planetary cores that start at 5 au migrated relatively short distances (by ≈ 2.5 au) by the time they reached their isolation mass. Thus, there may be a possibility that a planetary core can form almost *in situ* in some parts of the disc if core growth proceeds by concurrent accretion of multiple pebble species.

Analogous to the core growth saturation points discussed above, the points where the curves in Fig. 9 flatten mark the orbital distance at which the cores reached their isolation mass. We remind the reader here that we did not include type II migration, which might significantly change the final orbits of the planets.
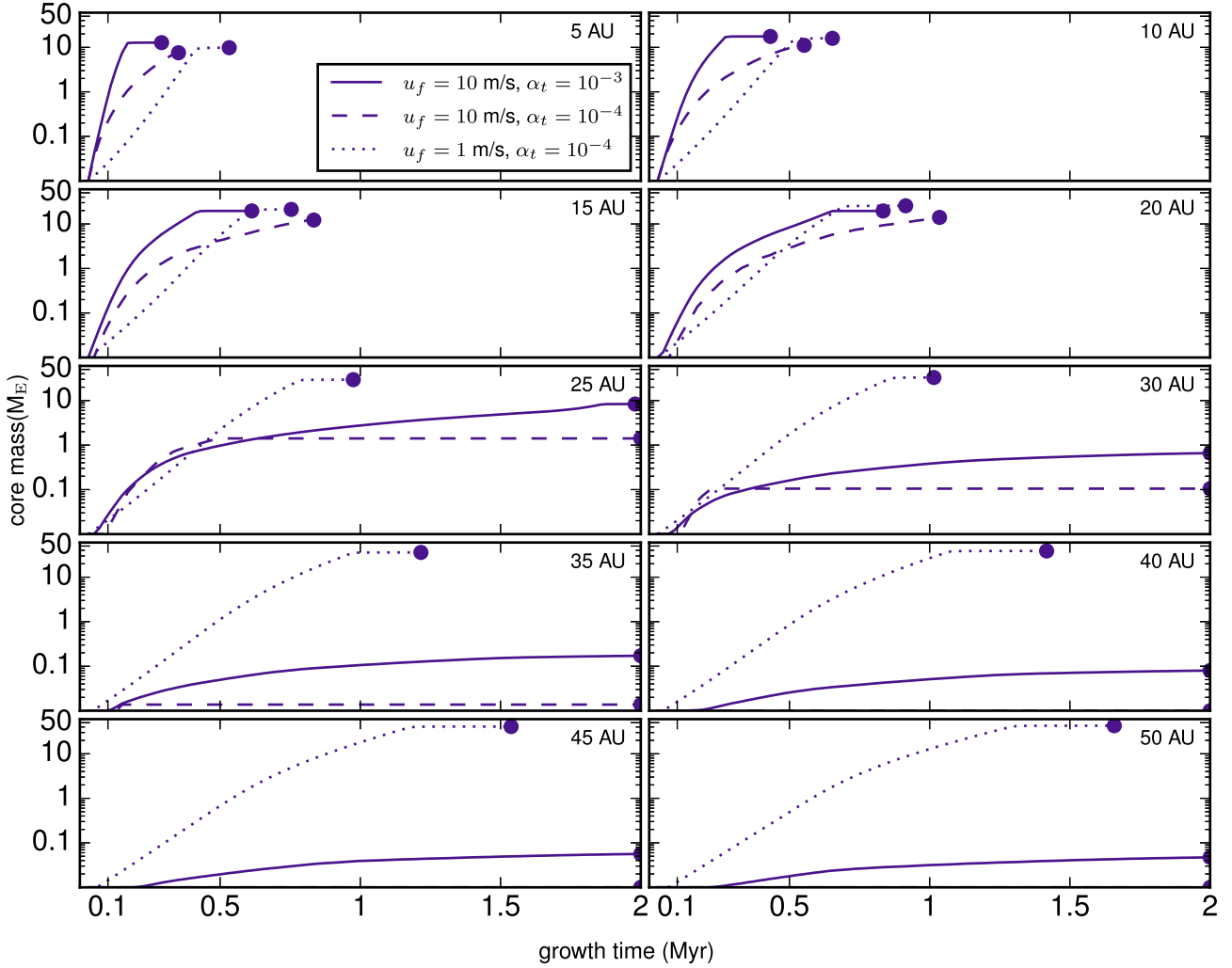
Figure 8. The growth time of the cores in Fig. 6 that grow by accretion of the multiple pebble species paradigm for nominal $f_{DG} = 0.01$, with the starting positions of planetary embryos shown on each plot. Some planetary cores grow very fast initially, and then the growth quickly stalls, as shown by the horizontal lines. Along the horizontal line, the planet is accreting pebble species with the smallest Stokes numbers, which have insignificant contribution to the core mass.
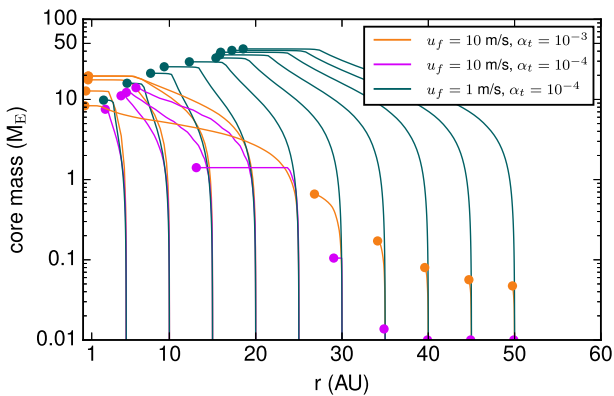

Figure 9. The growth tracks of the cores in Fig. 6 for nominal $f_{DG} = 0.01$. The solid lines show the evolution of the orbital position and the filled circles indicate the final masses and positions of the cores. The horizontal migration tracks show that the planet is accreting pebble species with the smallest Stokes numbers and does not significantly increase in mass, as it continues to migrate.

In our simulations, we were interested in core growth and thus did not model gas accretion as well as transition from type I to type II migration. Type II migration could be triggered during the gas accretion phase after the cores have reached their full pebble isolation mass. We envision that with the inclusion of type II migration, orbital decay is enhanced and could be significant to the extent that planets are lost to the host star, unless slower migration mechanisms are considered, such as the dynamical torque (Paardekooper 2014) and slower type II migrations (as in Crida & Bitsch 2017; Crida et al. 2017; Robert et al. 2018; Bergez-Casalou et al. 2020; Ndugu et al. 2021). Therefore, even though our simple multispecies accretion model shortens the growth time of cores, the orbital dilemma of the migration of gas giant planets needs to be explored further in the accretion of multiple pebble species. We shall investigate this in our upcoming work. However, a promising solution is the heating torque (Benítez-Llambay et al. 2015), which could prevent loss of planets to the central star by stopping inward migration, and this allows planet formation closer to the star.

4.4 The role of pebble isolation mass

The new formulation of pebble isolation mass in equation (22) functionally depends on several parameters, including the turbulence strength and pebble Stokes number; it relates to the pebble Stokes number in such way that $M_{iso,i} \propto (1/\tau_i)$. As a consequence of equation (22), we assume in our model that different pebble species are sequentially isolated by the growing planet when it starts to exert a pressure bump. This means that, in our model, pebbles with large Stokes numbers are trapped exterior the planet's orbit first, and those with small Stokes numbers are blocked last. We remind the reader that we did not model the pressure bump due to the growing planet. This would require modelling a complex gap profile that is anchored self-consistently to viscous disc evolution as in Dullemond et al. (2018), which is out of the scope of this study and will be considered in future works.

As we illustrated in Figs 2 and 7, pebbles may likely be blocked preferentially according to their sizes as a consequence of the pebble isolation prescription of B2018. For example, from both Figs 2 and 7, all pebble species to the right of the vertical line are blocked at the planetary mass indicated on the line.

From the above notion, the planet then reaches different isolation masses corresponding to each pebble species. At each pebble isolation stage, the planet continues to accrete smaller pebbles that are able to diffuse through the pressure bump that it generates, resulting in sustained core growth. However, when most of the pebbles have been blocked, the pebble accretion rate drops as the planet continues to slowly accrete the remaining small pebble species. For example, from Fig. 9, for the parameter set of $u_f = 1 \, \mathrm{m \, s^{-1}}$ and $\alpha_t = 10^{-4}$, a planetary seed planted at 50 au reaches its final core mass of $\sim 40 \, M_E$ at around 20 au, at which pebble isolation mass ranges from 33–47 M_E for pebbles with a Stokes number in the range 0.001–0.1 (see Fig. 7). Before that, as seen in Fig. 9, the accretion rate drops at around 30 au without any significant increase in mass. This is because from 30 au down to 20 au the planet is now slowly accreting small pebble species whose isolation mass is still high, while the majority of the other pebble species have been blocked. Finally, the planet reaches an isolation mass that roughly corresponds to isolation mass of $\sim 40 \, M_E$ for pebble species of approximately 0.02–0.1 cm at 20 au, as shown in Fig. 7.

As shown in Fig. 7, the pebble isolation mass spans a wide range of values. We observe here that relatively large pebble species in the distribution need very similar pebble isolation mass in order to be blocked. However, the millimetre-sized pebbles have a broader range of pebble isolation mass needed to block each species. This suggests that a planet may reach pebble isolation mass only once it is accreting predominantly large-size pebble species. In contrast, the planet may need to reach different isolation mass corresponding to each pebble species if the distribution is dominated by small-size pebble species.

The distributions in Fig. 7 further suggest that centimetre-sized pebbles produce relatively smaller cores as they are isolated at relatively low planetary masses compared with the smaller millimetre-sized pebbles. Thus, this suggests that building larger cores requires the presence of small-size pebbles, typically in the millimetre range, but more growth time will be needed to reach pebble isolation mass (see Fig. 8). This would require either moderately turbulent discs with high fragmentation velocities or quiescent discs with low fragmentation velocities, both of which produce pebbles in millimetre–centimetre ranges.

Furthermore, building massive cores requires that we implant planetary cores at far orbital distances, as can be seen in Fig. 9.
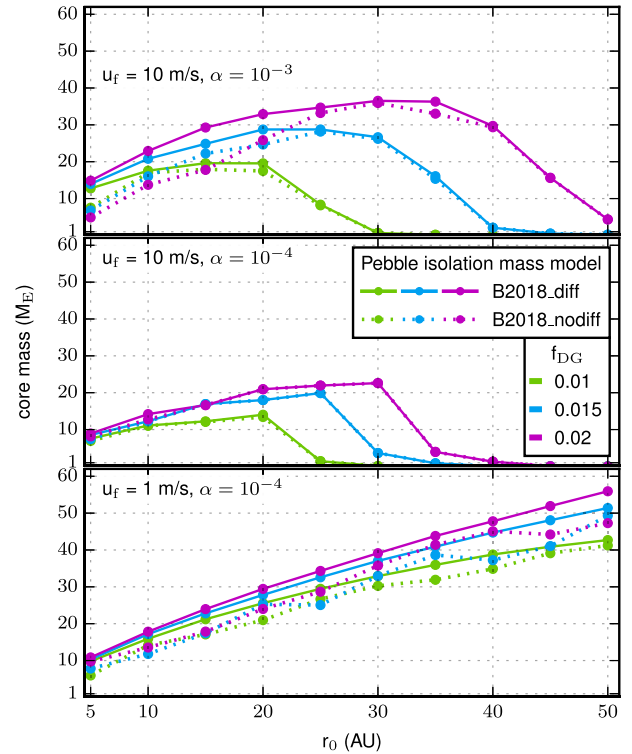

Figure 10. The dependence of core masses on turbulence strength and fragmentation velocity. B2018_diff and B2018_nodiff denote the pebble isolation mass models of B2018 with and without diffusion, respectively.

This enables the planet to continue accreting before it reaches pebble isolation mass, which scales not only with pebble size but also orbital distance, as in Fig. 7. However, there appears to be a problem of fast planet migration that mostly drives the planet to the inner discs, unless type I migration rates are slowed via mechanisms such as dynamical torques, as in Ndugu et al. (2021). As demonstrated here, fast core growth via the multiple pebble accretion paradigm could also provide another pathway for the planet to reach high pebble isolation mass before it migrates rapidly to inner disc regions where the isolation mass is smaller. Such fast core growths can allow the planet to beat the rapid type I migration, as suggested in Johansen et al. (2019).

The combination of millimetre–centimetre size distribution thus has two main advantages: the centimetre-size species initially offer high accretion rates that enable the planet to rapidly become massive enough to accrete the smaller species more efficiently; the small species survive much longer in the disc and hence there is a steady supply of material. This can then result in massive cores if multiple pebble accretion is taken into account together with diffusion as a determinant for the pebble isolation mass.

The influence of turbulent diffusion in the context of the multiple pebble accretion model is demonstrated in Fig. 10. From the top panel of Fig. 10, there is a significant difference in final core masses resulting from models with and without diffusion, especially in disc regions inside 20 au. However, at wider initial growth locations, the planet has the same mass regardless of the pebble isolation mass model used, as shown in the top panel of Fig. 10. In this case, the grain sizes may have similar isolation mass, as previous discussed.

In the case of $u_f = 10 \, \mathrm{m \, s^{-1}}$ and $\alpha_t = 10^{-4}$, as shown in the middle panel of Fig. 10, the difference between the pebble isolation mass

schemes with and without diffusion is marginal. This is because, as already mentioned before, grain sizes are generally bigger at high fragmentation velocities, and with low turbulence such large pebbles may not easily diffuse across the pressure bump generated by the planet. This means the dependence of the final core mass on isolation mass for larger pebbles species may turn out to be inconsequential. However, for the same turbulence strength of $\alpha_t = 10^{-4}$ and a lower fragmentation velocity of $u_f = 1 \text{ m s}^{-1}$, the effect of the diffusion of pebble isolation mass is still manifested, as shown in the bottom panel of Fig. 10. This is because low fragmentation velocities keep grain sizes small, which may be able to diffuse much more easily in a less turbulent disc compared with larger grains.

Considering the sequential isolation of pebbles as discussed above, as more and more pebbles are trapped outside the planet's orbit, the dust-to-gas ratio and pebble flux would ultimately reduce in the inner disc. This would affect the growth of planetary cores interior to the planet's orbit. In the outer orbit of the planet, the pile-up of pebbles enhances the dust-to-gas ratio at the pressure bump. This could trigger streaming instability and subsequent formation of planetesimals, thus reducing the amount of drifting pebbles, including those that would possibly diffuse through the pressure bump. This can then lead to reduced multiple pebble accretion rates and hence low-mass cores.

If the idea that smaller pebbles may overcome the pressure bump holds, then their conversion into planetesimals at the pressure bump together with the other species would affect the accretion rate of the smaller pebbles. But the planetesimals formed may be potential targets for accretion by the planet. However, in our simulations we ignored the possible conversion of pebbles into planetesimals at the pressure bump, which may play a key role in the mass budget of the inward drifting pebbles. Here we instead focused on how the diffusion of smaller pebbles affects core growth rates.

In the light of the novel flow isolation mass (Rosenthal & Murray-Clay 2020), we envisage that our results could substantially change. In particular, the flow isolation mass would limit the accretion of smaller, tightly coupled pebbles as they begin to interact with the planet's atmosphere, and may simply flow past the planet without being accreted. Consequently, the final core masses would then be restricted to the isolation mass of the larger pebbles, which could be lower than the values reported here. Future comprehensive planet population synthesis studies should consider detailed comparison between the existing pebble isolation criterion and the flow mass paradigm in explaining the existing features of the observed gas giant planets.

4.5 Giant planet core formation

Our results suggest that it is very challenging to form cores of giant planets when pebbles are much more coupled to the gas, for instance with $\tau_i \lesssim 0.001$, in agreement with Johansen et al. (2019). Such pebbles tend to follow gas streamlines and to interact poorly, gravitationally, with the protoplanets, making their capture difficult (for pebble capturing efficiencies by protoplanets, see Guillot et al. 2014). Furthermore, B2018 have demonstrated that reaching pebble isolation mass for tightly coupled pebbles requires cores as massive as 50 M_E. Reaching such a high core mass may prove difficult in the framework of dominant species, whose performance we have not rigorously tested here.

The *Jupiter Near-polar Orbiter* (*JUNO*) mission provided precise measurements of Jupiter's gravitational field, which has enabled better estimates of core masses. For instance, Jupiter's core mass was estimated to be 7–25 M_E (Wahl et al. 2017) while Debras &

Chabrier (2019) estimated 25–30 M_E and 30–45 M_E for non-compact and compact Jupiter cores, respectively. Other studies have inferred similar core masses for Solar system gas giants: for Jupiter, 10–40 M_E (Guillot 1999) and 37 M_E (Thorngren et al. 2016); for Saturn, 20–30 M_E (Guillot 1999) and 27 M_E (Thorngren et al. 2016). Many models have considered giant impacts to account for Jupiter's highly enriched core with heavy elements (e.g. Liu et al. 2019; Ginzburg & Chiang 2020). We have tested that it is quite challenging to obtain such high core masses using the classical pebble accretion model adopted in this work, unless we at least unphysically increase pebble concentration and consider discs with longer lifetimes. Moreover, the cores of giant planets that migrated to <10 au could have started their growth between 15–30 au (Johansen et al. 2019). In this orbital domain, we found it difficult to grow cores to masses above 25–30 M_E without evoking accretion of multiple pebble species. Therefore, we think that through our multiple pebble accretion scheme, massive cores of gas planets can form that match the results of the *JUNO* mission.

5 CONCLUSION

In this work, we have extended the pebble accretion paradigm, where core growth proceeds by concurrent accretion of multiple pebble species. We took into account the dependence of pebble isolation mass on turbulence parameter and pebble size. In our model, the final planetary core masses were set by the planet mass needed to block the smallest sized pebble species in the distribution of grain sizes under consideration. We self-consistently reconstructed grain distribution throughout the core growth process using the reconstruction model of Birnstiel et al. (2015). For the dust evolution, we employed the two-population model of Birnstiel et al. (2012).

Our simulations yielded a diversity of planetary cores with a wide range of core masses. The final outcome of core masses is primarily dictated by a combination of the dust-to-gas ratio, fragmentation velocities and turbulence strength that underpin the size distributions. Under a suitable set of disc conditions, cores of gas giants can form at orbits as far out as 50 au.

Our work has several other important consequences. First, recent studies (Wahl et al. 2017; Debras & Chabrier 2019) modelled Jupiter's core to contain heavy elements totalling 25–45 M_E, adding a further constraint on core accretion models. It is difficult to invoke pebble accretion to explain such a massive core build-up. Moreover, within the limitations of our numerical simulations, we could not easily build massive cores well above ∼30 M_E using the classical scenario of dominant species. If we are to invoke pebble accretion to explain the assembly of such massive cores, then our model of concurrent accretion of multiple pebble species would provide a possible mechanism to explain this enigma.

Secondly, in the study of metallicity correlation of extrasolar planets, Guillot et al. (2006) found that their sample planets contained ∼20–100 M_E in heavy elements. The work of Thorngren et al. (2016) also suggests a strong correlation between the planetary mass and the amount of heavy elements accreted by the planet. If these results are confirmed, then the accumulation of such a large amount of heavy material is in conflict with the classical core accretion model of planet formation. However, some recent solutions have been proposed; for example, the merger of giant planets via collisions (Liu et al. 2019; Ginzburg & Chiang 2020) or the accretion of the evaporated material may increase the heavy element content of the giant planets (Schneider & Bitsch 2021).

Another important aspect of classical core accretion that we did not account for in this study is the accretion of planetesimals. Al-

though gas giant planet cores form with difficulties via planetesimal accretion, the capture of planetesimals by the planet can also enrich the planet with heavy elements (Shibata & Ikoma 2019; Shibata, Helled & Ikoma 2020; Venturini & Helled 2020). Nevertheless, as we have demonstrated here, it is possible that these planets consumed several different dust species if their formation proceeded through the pebble accretion paradigm, and can form such massive gas giant planet cores even at the disc's outskirts.

Thirdly, a diversity of gaps and rings over a wide orbital regime has been discovered in many discs through the Atacama Large Millimeter/submillimeter Array (ALMA) programme (e.g. Huang et al. 2018a; Huang et al. 2018b,c; Long et al. 2018) and the Disk Substructures at High Angular Resolution Project (DSHARP; e.g. Andrews et al. 2018). Planet–disc interactions have been evoked as one possible way to explain the occurrence of these structures, though this is subject to discussion (Ndugu et al. 2019). Recently, in a sample of 16 ALMA discs studied by van der Marel et al. (2019), the authors found some substructures at orbital distances far beyond 30 au, and found evidence for the presence of massive planets at those orbital distances. An important question as to whether or not these substructures are indeed caused by growing planets has been put forth (e.g. Lodato et al. 2019; Ndugu et al. 2019). If it is true that planets may be responsible for opening gaps at such wider orbital distances, then the existing core accretion models are missing important ingredients for explaining the formation of planets at these remote locations. It is, however, possible to form gas giant planets at these wide orbits if: (i) concurrent accretion of multiple pebble species is taken into account; (ii) it is assumed that the giant planets at such wide orbits form via the gravitational instability paradigm (Boss 1997; Boley 2009; Armitage 2010); and (iii) the observed rings are assumed to be caused by other phenomena, such as MRI, than ongoing planet formation. The rings could, in turn, be hotspots for planet formation at such wide orbits (Morbidelli 2020). Thus, the precise explanation for the origin of the observed gaps/rings at wider orbits is a complicated one, more like a 'chicken and egg' problem.

Although our model has shed some light on the formation of massive giant planets at wider orbits of discs, it did not capture important planet formation aspects such as the competition of multiple cores for the available building blocks and orbital manipulation by *N*-body interactions between cores. We therefore recommend that future models that study multiple pebble species accretion consider core growth competition and the *N*-body paradigm for a detailed and substantial explanation of the formation of gas giant planets at wider orbits.

ACKNOWLEDGEMENTS

DATA AVAILABILITY

For the purpose of reproducibility, the code used to obtain results in this paper will be provided upon reasonable request.

REFERENCES

Adachi I., Hayashi C., Nakazawa K., 1976, Progress of Theoretical Physics, 56, 1756
Alexander R. D., Armitage P. J., 2007, MNRAS, 375, 500
Andrews S. M. et al., 2018, ApJ, 869, L41
Ansdell M., Williams J. P., Manara C. F., Miotello A., Facchini S., van der Marel N., Testi L., van Dishoeck E. F., 2017, AJ, 153, 240
Armitage P., 2010, Astrophysics of Planet Formation. Cambridge Univ. Press, Cambridge
Ataiee S., Baruteau C., Alibert Y., Benz W., 2018, A&A, 615, A110
Barrière-Fouchet L., Gonzalez J. F., Murray J. R., Humble R. J., Maddison S. T., 2005, A&A, 443, 185
Baruteau C. et al., 2014, in Beuther H., Klessen R. S., Dullemond C. P., Henning T., eds, Protostars and Planets VI. University of Arizona Press, Tucson, AZ, p. 667
Benítez-Llambay P., Masset F., Koenigsberger G., Szulágyi J., 2015, Nature, 520, 63
Bergez-Casalou C., Bitsch B., Pierens A., Crida A., Raymond S. N., 2020, A&A, 643, A133
Birnstiel T., Dullemond C. P., Brauer F., 2009, A&A, 503, L5
Birnstiel T., Dullemond C. P., Brauer F., 2010, A&A, 513, A79
Birnstiel T., Ormel C. W., Dullemond C. P., 2011, A&A, 525, A11
Birnstiel T., Klahr H., Ercolano B., 2012, A&A, 539, A148
Birnstiel T., Andrews S. M., Pinilla P., Kama M., 2015, ApJ, 813, L14
Bitsch B., Johansen A., 2017, in Formation, Evolution, and Dynamics of Young Solar Systems, ASSL Vol. 445. Springer, Berlin, p. 339
Bitsch B., Lambrechts M., Johansen A., 2015, A&A, 582, A112
Bitsch B., Morbidelli A., Johansen A., Lega E., Lambrechts M., Crida A., 2018, A&A, 612, A30 (B2018)
Blum J., Wurm G., 2008, ARA&A, 46, 21
Boley A. C., 2009, ApJ, 695, L53
Boss A. P., 1997, Science, 276, 1836
Bottke W. F., Durda D. D., Nesvorný D., Jedicke R., Morbidelli A., Vokrouhlický D., Levison H., 2005a, Icarus, 175, 111
Bottke W. F., Durda D. D., Nesvorný D., Jedicke R., Morbidelli A., Vokrouhlický D., Levison H. F., 2005b, Icarus, 179, 63
Brauer F., Dullemond C. P., Johansen A., Henning T., Klahr H., Natta A., 2007, A&A, 469, 1169
Brauer F., Dullemond C. P., Henning T., 2008, A&A, 480, 859
Brügger N., Alibert Y., Ataiee S., Benz W., 2018, A&A, 619, A174
Cameron A. G. W., 1978, Moon and Planets, 18, 5
Carrasco-González C. et al., 2016, ApJ, 821, L16
Carrera D., Johansen A., Davies M. B., 2015, A&A, 579, A43
Coleman G. A. L., Nelson R. P., 2014, MNRAS, 445, 479
Crida A., Bitsch B., 2017, Icarus, 285, 145
Crida A., Bitsch B., Ndugu N., Morbidelli A., 2017, in European Planetary Science Congress. p. EPSC2017–44
Debras F., Chabrier G., 2019, ApJ, 872, 100
Dominik C., Dullemond C. P., 2008, A&A, 491, 663
Drążkowska J., Li S., Birnstiel T., Stammler S. M., Li H., 2019, ApJ, 885, 91
Drążkowska J., Stammler S. M., Birnstiel T., 2021, A&A, 647, A15
Dullemond C. P., Dominik C., 2004, A&A, 421, 1075
Dullemond C. P., Dominik C., 2005, A&A, 434, 971
Dullemond C. P. et al., 2018, ApJ, 869, L46
Durisen R. H., Boss A. P., Mayer L., Nelson A. F., Quinn T., Rice W. K. M., 2007, in Reipurth B., Jewitt D., Keil K., Protostars and Planets V. University of Arizona, Tuscon, AZ, p. 607
Dzyurkevich N., Flock M., Turner N. J., Klahr H., Henning T., 2010, A&A, 515, A70
Gammie C. F., 2001, ApJ, 553, 174
Garaud P., Barrière-Fouchet L., Lin D. N. C., 2004, ApJ, 603, 292
Ginzburg S., Chiang E., 2020, MNRAS, 498, 680
Guilera O. M., Sándor Z., Ronco M. P., Venturini J., Miller Bertolami M. M., 2020, A&A, 642, A140
Guillot T., 1999, Planetary and Space Science, 47, 1183

Guillot T., Santos N. C., Pont F., Iro N., Melo C., Ribas I., 2006, A&A, 453, L21

Guillot T., Ida S., Ormel C. W., 2014, A&A, 572, A72

Gundlach B., Blum J., 2015, ApJ, 798, 34

Gundlach B., Kilias S., Beitz E., Blum J., 2011, Icarus, 214, 717

Huang J. et al., 2018a, ApJ, 852, 122

Huang J. et al., 2018b, ApJ, 869, L42

Huang J. et al., 2018c, ApJ, 869, L43

Johansen A., Bitsch B., 2019, A&A, 631, A70

Johansen A., Lacerda P., 2010, MNRAS, 404, 475

Johansen A., Oishi J. S., Mac Low M.-M., Klahr H., Henning T., Youdin A., 2007, Nature, 448, 1022

Johansen A., Youdin A., Klahr H., 2009, ApJ, 697, 1269

Johansen A., Klahr H., Henning T., 2011, A&A, 529, A62

Johansen A., Blum J., Tanaka H., Ormel C., Bizzarro M., Rickman H., 2014, in Beuther H., Klessen R. S., Dullemond C. P., Henning T., eds, Protostars and Planets VI. University of Arizona, Tuscon, AZ, p. 547

Johansen A., Ida S., Brasser R., 2019, A&A, 622, A202

Kokubo E., Ida S., 1998, Icarus, 131, 171

Kokubo E., Ida S., 2012, Progress of Theoretical and Experimental Physics, 2012, 01A308

Kuiper G. P., 1951, pnas, 37, 1

Lambrechts M., Johansen A., 2012, A&A, 544, A32

Lambrechts M., Johansen A., 2014, A&A, 572, A107

Lambrechts M., Johansen A., Morbidelli A., 2014, A&A, 572, A35 (L2014)

Levison H. F., Thommes E., Duncan M. J., 2010, AJ, 139, 1297

Liu S-F., Hori Y., Müller S., Zheng X., Helled R., Lin D., Isella A., 2019, Nature, 572, 355

Lodato G. et al., 2019, MNRAS, 486, 453

Long F. et al., 2018, ApJ, 869, 17

Lynden-Bell D., Pringle J. E., 1974, MNRAS, 168, 603

Manara C. F., Mordasini C., Testi L., Williams J. P., Miotello A., Lodato G., Emsenhuber A., 2019, A&A, 631, L2

Mathis J. S., Rumpl W., Nordsieck K. H., 1977, ApJ, 217, 425

Mizuno H., 1980, Progress of Theoretical Physics, 64, 544

Mizuno H., Nakazawa K., Hayashi C., 1978, Progress of Theoretical Physics, 60, 699

Morbidelli A., 2020, A&A, 638, A1

Morbidelli A., Nesvorny D., 2012, A&A, 546, A18

Morbidelli A., Bottke W. F., Nesvorný D., Levison H. F., 2009, Icarus, 204, 558

Morbidelli A., Lambrechts M., Jacobson S., Bitsch B., 2015, Icarus, 258, 418

Mordasini C., Alibert Y., Benz W., 2009a, A&A, 501, 1139

Mordasini C., Alibert Y., Benz W., Naef D., 2009b, A&A, 501, 1161

Musiolik G., Wurm G., 2019, ApJ, 873, 58

Nakagawa Y., Sekiya M., Hayashi C., 1986, Icarus, 67, 375

Nayakshin S., 2010, MNRAS, 408, L36

Nayakshin S., Dipierro G., Szulágyi J., 2019, MNRAS, 488, L12

Ndugu N., Jurua E., Bitsch B., 2018, MNRAS, 474, 886

Ndugu N., Bitsch B., Jurua E., 2019, MNRAS, 488, 3625

Ndugu N., Bitsch B., Morbidelli A., Crida A., Jurua E., 2021, MNRAS, 501, 2017

Ormel C. W., Klahr H. H., 2010, A&A, 520, A43

Paardekooper S.-J., 2014, MNRAS, 444, 2031

Paardekooper S.-J., Mellema G., 2006, A&A, 459, L17

Paardekooper S.-J., Baruteau C., Crida A., Kley W., 2010, MNRAS, 401, 1950

Paardekooper S.-J., Baruteau C., Meru F., 2011, MNRAS, 416, L65

Pérez L. M. et al., 2012, ApJ, 760, L17

Pinilla P., Birnstiel T., Ricci L., Dullemond C. P., Uribe A. L., Testi L., Natta A., 2012, A&A, 538, A114

Raettig N., Klahr H., Lyra W., 2015, ApJ, 804, 35

Rafikov R. R., 2005, ApJ, 621, L69

Rice W. K. M., Armitage P. J., Bonnell I. A., Bate M. R., Jeffers S. V., Vine S. G., 2003, MNRAS, 346, L36

Robert C. M. T., Crida A., Lega E., Méheut H., Morbidelli A., 2018, A&A, 617, A98

Rodmann J., Henning T., Chandler C. J., Mundy L. G., Wilner D. J., 2006, A&A, 446, 211

Rosenthal M. M., Murray-Clay R. A., 2020, ApJ, 898, 108

Safronov V., 1969, Evolution of Protoplanetary Cloud and Formation of the Earth and the Planets. Keter, Jerusalem

Savvidou S., Bitsch B., 2021, A&A, 650, A132

Savvidou S., Bitsch B., Lambrechts M., 2020, A&A, 640, A63

Schneider A. D., Bitsch B., 2021, A&A, 654, A71

Shibata S., Ikoma M., 2019, MNRAS, 487, 4510

Shibata S., Helled R., Ikoma M., 2020, A&A, 633, A33

Singer K. N. et al., 2019, Science, 363, 955

Takeuchi T., Lin D. N. C., 2005, ApJ, 623, 482

Tanaka H., Ida S., 1999, Icarus, 139, 350

Tanga P., Weidenschilling S. J., Michel P., Richardson D. C., 2004, A&A, 427, 1105

Testi L., Natta A., Shepherd D. S., Wilner D. J., 2003, A&A, 403, 323

Testi L. et al., 2014, in Beuther H., Klessen R. S., Dullemond C. P., Henning T., eds, Protostars and Planets VI. University of Arizona, Tuscon, AZ, p. 339

Thommes E. W., Duncan M. J., Levison H. F., 2003, Icarus, 161, 431

Thorngren D. P., Fortney J. J., Murray-Clay R. A., Lopez E. D., 2016, ApJ, 831, 64

Trotta F., Testi L., Natta A., Isella A., Ricci L., 2013, A&A, 558, A64

Tychoniec Ł. et al., 2020, A&A, 640, A19

Uribe A. L., Klahr H., Flock M., Henning T., 2011, ApJ, 736, 85

van der Marel N., Dong R., di Francesco J., Williams J. P., Tobin J., 2019, ApJ, 872, 112

Venturini J., Helled R., 2020, A&A, 634, A31

Venturini J., Guilera O. M., Ronco M. P., Mordasini C., 2020, A&A, 644, A174

Wada K., Tanaka H., Suyama T., Kimura H., Yamamoto T., 2008, ApJ, 677, 1296

Wahl S. M. et al., 2017, Geophys. Res. Lett., 44, 4649

Weber P., Benítez-Llambay P., Gressel O., Krapp L., Pessah M. E., 2018, ApJ, 854, 153

Weidenschilling S. J., 1977, MNRAS, 180, 57

Wetherill G. W., 1980, ARA&A, 18, 77

Whipple F. L., 1972, in Elvius A., ed., From Plasma to Planet. Wiley, New York, p. 211

Wilner D. J., D'Alessio P., Calvet N., Claussen M. J., Hartmann L., 2005, ApJ, 626, L109

Youdin A. N., Goodman J., 2005, ApJ, 620, 459

Youdin A. N., Lithwick Y., 2007, Icarus, 192, 588

APPENDIX A: THE DUST DISTRIBUTIONS AND MASS FRACTIONS

In Fig. A1, we show the variation of pebble surface density and the Stokes number as a function of grain for the dust size distribution reconstructed at radial distances 5, 10, 20 and 50 au, for $\alpha_t = 10^{-3}$, $u_f = 10 \, \mathrm{m \, s^{-1}}$ and $f_{DG} = 0.01$. On each plot, we show the fractions of pebbles that have Stokes number greater and less than 0.001. Grains with Stokes number ≥ 0.001 are shown by the shaded region. We also show the fractions of the large and small populations from the two-population model. In the two-population scheme, grain sizes are calculated and fixed by growth, fragmentation and drift limits. Here, in the inner and outer disc regions, the fragmentation and drift limits dominate, respectively with 0.75 and 0.97 of the mass constituting the large population. As shown in the plots, the reconstructed grain distributions with Stokes number ≥ 0.001 dominate in the inner disc regions, ≤ 30 au, which carry over 80 per cent of the mass, similar to the fractions of the model for two dust populations.

Furthermore, as shown in Fig. A1, very few grains have a Stokes number greater than 0.1, and most of the mass in the reconstructed grain distribution is carried by the population of grains with Stokes

number ≥ 0.001. In addition, the accretion of pebbles with Stokes number < 0.001 is generally inefficient as these pebbles are usually well coupled to the gas (Guillot et al. 2014), and we observed the same trend in our simulations. Thus, in our simulations, the embryos mostly accrete pebbles with Stokes number ≥ 0.001.

In Fig. A2, we show dust fractions as a function of radial distance for the different combinations of fragmentation velocities and turbulence strengths, and for both the simulated two-population model and the reconstructed grain size distributions. In the simulations with fragmentation velocity of $10 \mathrm{~m~s}^{-1}$, most of the mass is carried by grains with Stokes number ≥ 0.001 within 50 au, as shown by the panels in the first and second rows of Fig. A2. However, for the case of fragmentation velocity of $1 \mathrm{~m~s}^{-1}$, the fraction of pebbles with Stokes number ≥ 0.001 begins to approach that of the large population simulated using the model of two dust populations at orbital distances greater than 5 au. Here, within 5 au, pebbles with Stokes number less than 0.001 dominate. This may suggest a stronger fragmentation inside 5 au that produces smaller grains, which then have small Stokes numbers compared with other parts of the disc.

APPENDIX B: THE RECIPE FOR CONCURRENT ACCRETION OF MULTIPLE PEBBLE SPECIES

In this appendix, we give a brief description of the recipe that we used in our numerical simulations involving concurrent accretion of multiple pebble species in reference to the full-size distribution as in Birnstiel et al. (2012). It is a simple extension of the implementation of the single species model that can readily be adopted for other models of particle distribution. At each time snapshot and orbital distance referenced by j and k respectively, we implement core accretion of multiple pebble species as follows.

Step 1. Initialize planet mass, $M_{j=0, k=0}$, orbital distance, $r_{k=0}$.

Step 2. Calculate the disc parameters at r_k and time t_j.

Step 3. Obtain the logarithmic distribution of N pebble sizes $R_{i+1} = 1.12R_i$, as in Birnstiel et al. (2011).

Step 4. From the logarithmic particle size distribution, calculate the pebble surface density, $\Sigma_{\mathrm{peb},i}$, for each of the N species according

the reconstruction scheme in Birnstiel et al. (2015) and calculate the Stokes number, τ_i, for each species in the Epstein regime as

$$\tau_i = \frac{\rho_\bullet \pi R_i}{2\Sigma_\mathrm{g}}. \tag{B1}$$

Step 5. Calculate the pebble isolation mass for each species according to equation (22).

Step 6. If the planet mass is larger than the pebble isolation mass of pebble species with the smallest Stokes number in the size distribution, stop the time integration. This is because as the planet grows, pebbles with larger Stokes numbers are isolated first, while the ones with smaller Stokes numbers are isolated last, depending on the mass of the planet (see equation 22 and further explanation in B2018). Hence, the core mass is determined by the isolation mass of pebbles with the smallest Stokes numbers.

Step 7. If the planet mass is larger than the isolation mass of the ith species, stop accretion of the ith species. Otherwise, accrete the ith species by calculating the core accretion rate $\dot{M}_{\mathrm{core},i}$ using equations (14), (15) and (17).

Step 8. Calculate the total core growth rate by consolidating contributions from each species:

$$\dot{M}_{j,k} = \sum_i \dot{M}_{\mathrm{core},i}. \tag{B2}$$

Step 9. Calculate the new planet mass from

$$M_{j+1,k} = M_{j,k} + \dot{M}_{j,k}\delta t, \tag{B3}$$

where δt is the time-step.

Step 10. Calculate the migration rate and the new orbital location of the growing core.

Step 11. Increase time by δt and repeat from Step 2 until the condition in Step 6 is fulfilled.

This paper has been typeset from a TEX/LATEX file prepared by the author.
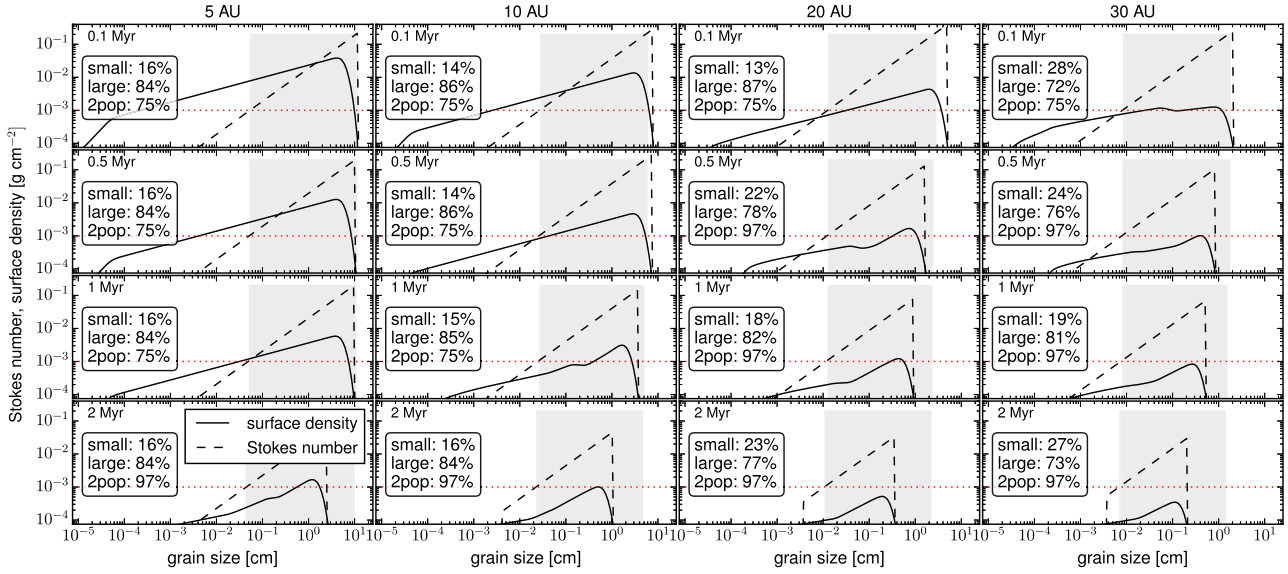
Figure A1. The grain surface density and Stokes number as a function of grain size reconstructed from the two-population model at 5, 10, 20 and 50 au at time 0.1, 0.5, 1 and 2 Myr. On the plots, we show the fractions of small and large grains that have Stokes numbers less and greater than 0.001, respectively. The shaded regions show large grains with Stokes number 0.001, which were mostly accreted in our growth model. Here, *2pop* is the fraction of the large dust population from the two-population simulations that contains most of the solid mass. The dust evolution was performed with $u_f = 10\,\mathrm{m\,s^{-1}}$, $\alpha_t = 10^{-3}$ and $f_{DG} = 0.01$ for 2 Myr.
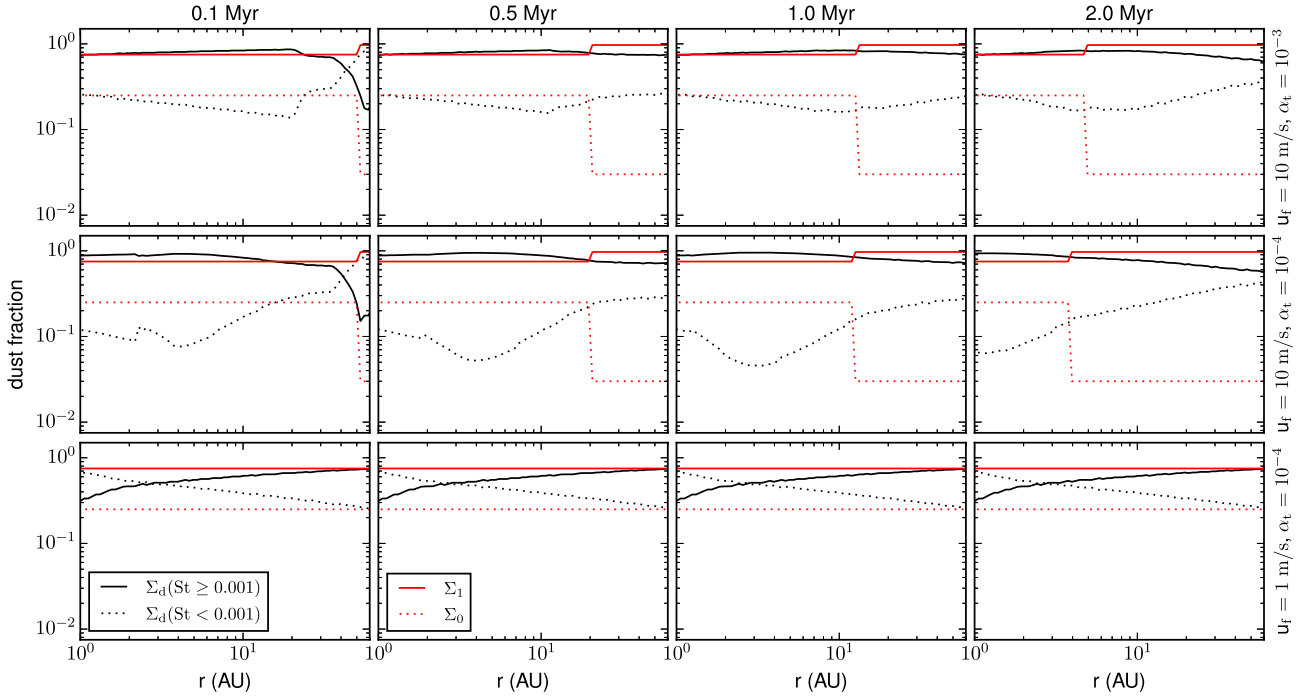

Figure A2. The radial mass fractions of small (with Stokes number < 0.001) and large (with Stokes number ≥0.001) grains. Σ_0 and Σ_1 are the small and large dust populations from the model of two dust populations. Each row shows simulations with different combinations of fragmentation velocity and turbulence strength, and an initial dust-to-gas ratio of $f_{DG} = 0.01$.